Fe catalysts for methane decomposition to produce hydrogen and carbon nano materials

Lu Zhou [a],*, Linga Reddy Enakonda [a],*, Moussab Harb [a], Youssef Saih [a], Antonio Aguilar-Tapia [a], Samy Ould-Chikh [a], Jean-louis Hazemann [b,c], Jun Li [d], Nini Wei [d], Daniel Gary [e], Pascal Del-Gallo [e], Jean-Marie Basset [a],*

[a] KAUST Catalysis Center, 4700 King Abdullah University of Science & Technology, Thuwal 23955-6900, Saudi Arabia
[b] BM30B/FAME beamline, ESRF, F-38043 Grenoble cedex 9, France
[c] Institut Néel, UPR 2940 CNRS, F-38042 Grenoble cedex 9, France
[d] Core Lab, King Abdullah University of Science and Technology, Thuwal 23955-6900, Saudi Arabia
[e] Paris Saclay Research Center, Materials Sciences, AIR LIQUIDE Research & Development, France

ARTICLE INFO

ABSTRACT

Conducting catalytic methane decomposition over Fe catalysts is a green and economic route to produce H_2 without CO/CO_2 contamination. Fused 65 wt% and impregnated 20 wt% Fe catalysts were synthesized with different additives to investigate their activity, whereas showing Fe-Al_2O_3 combination as the best catalyst. Al_2O_3 is speculated to expose more Fe^0 for the selective deposition of carbon nano tubes (CNTs). A fused Fe (65 wt%)-Al_2O_3 sample was further investigated by means of H_2-TPR, in-situ XRD, HRTEM and XAS to conclude 750 °C is the optimized temperature for H_2 pre-reduction and reaction to obtain a high activity. Based on density functional theory (DFT) study, a reaction mechanism over Fe catalysts was proposed to explain the formation of graphite from unstable supersaturated iron carbides decomposition. A carbon deposition model was further proposed which explains the formation of different carbon nano materials.
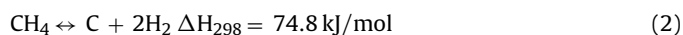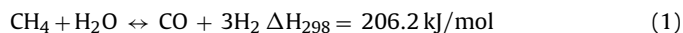
1. Introduction

Hydrogen, combined with fuel cells technology, is a promising vector for clean energy. Nowadays, the annual production of hydrogen is about 0.1 Gton/year. However, most of it is obtained from the steam reforming of fossil fuels, which inevitably emits a huge amount of CO_2 a well-known greenhouse gas. It is estimated that 60Mt H_2 today are produced from fossils fuels for ammonia and petrochemical, and this is emitting near 500 MT CO_2 [1,2].

Compared to traditional methane steam reforming (MSR, Eq. (1)), catalytic methane decomposition (CMD, Eq. (2)) is an ideal process to produce pure hydrogen without any contamination of CO/CO_2 [3–7]. Nevertheless, it should be pointed out here that, in a real CMD process, due to the reaction between methane and "oxygen" from the catalysts (support and/or metal oxides), the emission of CO/CO_2 in very low concentration cannot be avoided. We previously reported this formation of trace amount CO and CO_2 during

the initial two minutes during a CMD reaction over Ni catalyst [8]. Even though, it is reported that, the energy input requirements per mole of hydrogen for CMD is significantly less than that of MSR (37.8 and 63.3 kJ/mol H_2, respectively). This makes CMD a "greener" route than MSR to produce H_2.

$$CH_4 + H_2O \leftrightarrow CO + 3H_2 \quad \Delta H_{298} = 206.2\,kJ/mol \qquad (1)$$

$$CH_4 \leftrightarrow C + 2H_2 \quad \Delta H_{298} = 74.8\,kJ/mol \qquad (2)$$

Koerts et al. demonstrated that the rate of methane activation in the presence of metals decreased in the following order: Co, Ru, Ni, Rh > Pt, Re, Ir > Pd, Cu, W, Fe, Mo [9]. Over a series of oxidized diamond-supported metal catalysts, Ando et al. reported the CMD activity following the order: Ni > Pd > Fe, Co, Ru, Rh, Ir, Pt [10]. Therefore, Ni based catalysts are the most studied for CMD. CMD reaction over Ni based catalysts is often simplified as three key steps as methane activation, carbon nucleation and carbon deposition to grow carbon materials [11]. Methane molecules adsorb dissociatively on Ni metal surface (by a C—H bond activation process). It leads by further steps carbon atoms with a concomitant desorption of molecular hydrogen. The adsorbed carbon atoms diffuse on the surface or through the bulk of Ni metal particle to a

* Corresponding authors.
E-mail addresses: lu.zhou@kaust.edu.sa (L. Zhou), linga.enakonda@kaust.edu.sa (L.R. Enakonda), jeanmarie.basset@kaust.edu.sa (J.-M. Basset).

Table 1
Literature review of CMD over Fe based catalysts.

Sample	Preparation method	Loading	Reactor	Reduction condition	Reaction condition	Life time	CH_4 conv.	Ref.
Fe/MgO	impregnation	50 wt%	Fixed bed	700 °C, H_2	700 °C, CH_4, 6 L/g_{cat} h	150 min	45%	[24]
2Ni-1Fe-1Al	Co-precipitation	42 wt% Ni, 20 wt% Fe	Fixed bed	700 °C, H_2	650 °C, 30% CH_4/Ar, 42 L/g_{cat} h	150 h	40%	[25]
Fe/SiO$_2$	impregnation	10 wt%	Fixed bed	700 °C, 50% H_2/N_2	800 °C, 70% CH_4/N_2, 15 L/g_{cat} h	150 min	95%	[5]
Fe/MgO	impregnation	10 wt%	Fixed bed	700 °C, 50% H_2/N_2	800 °C, 70% CH_4/N_2, 15 L/g_{cat} h	200 min	25%	[5]
Fe/Al$_2$O$_3$	fusion	53 wt%	Fluidized bed	750 °C, H_2	700 °C, CH_4, 6 L/g_{cat} h	6 h	18%	[26]
Ni-Fe-SiO$_2$	Sol-gel	65 wt% Ni, 10 wt% Fe	Fixed bed	650 °C, H_2	550 °C, CH_4, 30 L/g_{cat} h	400 min	16%	[27]
FeMo/MgO	fusion	62 wt% Fe, 16 wt% Mo	Fixed bed	550 °C, H_2	800 °C, CH_4, 1 L/g_{cat} h	200 min	92%	[28]
Fe/CeO$_2$	Co-precipitation	56 wt%Fe	Fixed bed	750 °C, 4% H_2/Ar	750 °C, 30% CH_4/Ar, 1.2 L/g_{cat} h	150 min	25%	[29]
Fe-Cu	Raney type	50 wt%Fe	Fixed bed	600 °C, 10% H_2/N_2	600 °C, 10% CH_4/N_2, 6.6 L/g_{cat} h	200 min	30%	[30]

suitable area for the formation of graphene sheets formation. We previously concluded that the Ni size together with the Ni and support interaction would strongly affect the formation of different types of carbon materials including carbon nano tubes (CNTs), carbon nano onions (CNOs) and Carbon nano fibers (CNFs) [8]. Recent years, Shen and Lua [5] discussed in detail CMD performance in terms of methane conversion, carbon yield and carbon morphologies over Ni and Ni–Cu alloys with various atomic ratios supported on CNTs. The Ni$_{78}$Cu$_{22}$/CNT catalyst exhibited the best catalytic performance with a stable methane conversion of 80% and a carbon yield of 602 g_C/g_{Ni} at 700 °C. Kang et al. [6] synthesized a nickel–carbon–B$_2$O$_3$ core–shell catalysts, which showed excellent CMD activity at 750 °C. A special CMD mechanism was also proposed to explain this catalyst good CMD activity and stability. While generating CNOs, the encapsulated nickel core by carbon deposition was easily escaped through the initial amorphous carbon shell before being deactivated. The escaped nickel particle was re-used to produce hydrogen and new CNOs while the remaining CNOs without the nickel core were observed in the hollow form.

However, unlike the MSR which is already industrialized and can be operated for couple of years, the CMD run period is rather short due to the catalysts deactivation by carbon deposition to block the catalyst pores and/or completely encapsulate the metal and/or plug the reactor. The longest lifetime of reported CMD catalyst is about 200 h over Ni based catalysts [12]. In most literatures, researchers are trying to regenerate the deactivated Ni catalysts by steam regeneration and/or air regeneration [13–18]. Nevertheless, it is obvious that these regenerations will produce CO/CO$_2$, which will play against the 'green' character of the CMD process. To improve the catalysts life, Ni mixed with Cu, Fe, Co, and/or Pd catalysts were investigated in literatures [19–23], whilst none promising results has been reported until now.

Therefore, to make the CMD real green and economic, using a very cheap catalyst to decompose methane into hydrogen and without regeneration of the spent catalyst and carbon materials mixtures, is probably a reasonable approach. Fe, also has the partially filled 3d orbitals to facilitate the hydrocarbon dissociation via partially accepting electrons, is thus a good candidate for this purpose. Fe is known to be more environmental friendly, whilst the price of Fe is just 1/200 of that of Ni. Moreover, due to the higher melting point of Fe than Ni, it is found that Fe catalysts can operate at higher temperature (700–950 °C) than Ni catalysts (500–700 °C). This can thus lead to a better thermodynamic conversion on Fe catalysts than Ni catalysts, because CMD is an endothermic reaction.

There are some studies about CMD over Fe based catalysts summarized in Table 1. Because of different selections of supports, preparation methods, additives and reaction conditions, the cat-

alysts performances in regarding of methane conversion and life time among all these studies are different from each other. There is still no agreement on Fe catalysts composition and reaction condition optimization for CMD reaction. In the present work, we try to approach the problem by a systematic and comparative study using both fusion and impregnation methods. Doing so, we synthesized a variety of Fe-based catalysts to thoroughly investigate the effect of supports, additives, activation methods and reaction conditions on their CMD performances.

2. Experimental

2.1. Catalysts preparation

Fe(NO$_3$)$_3$·9H$_2$O, Al(NO$_3$)$_3$·9H$_2$O, Mg(NO$_3$)$_2$·6H$_2$O, Ce(NO$_3$)$_3$·6H$_2$O, Cu(NO$_3$)$_2$·3H$_2$O, Co(NO$_3$)$_2$·6H$_2$O, Ca(NO$_3$)$_2$·4H$_2$O and N$_4$O$_{12}$Ti·4H$_2$O were used respectively as precursors for Fe, Al, Mg, Ce, Cu, Ca and Ti. A fusion method described in our previous study [31], was used here to prepare Fe based catalysts by directly calcining above mentioned Fe precursor with one or two other metal nitrate precursors at 450 °C for 3 h. The prepared catalysts are named as f-Fe$_x$-M$_y$, while f means fusion method, M represents additives, x and y are the loading of Fe, M respectively. For example, f-Fe$_{65}$-Al$_{3.7}$ means a fused catalyst with 65 wt% Fe and 3.7 wt% Al, the remains are the oxygen. On the other hand, the fusion method is also applied to prepare one metal catalyst, which is designed as f-M (M is the element). For example, f-Mg means pure MgO sample.

The impregnation method with Fe(NO$_3$)$_3$·9H$_2$O solution was also used in this work to prepare supported Fe catalysts. After impregnation, the samples were dried at 110 °C for overnight and then calcined at 450 °C for 3 h. The obtained catalysts are designed as I-Fe$_x$-S. The I means the impregnation method, x is the Fe loading, while S means the support from γ-Al$_2$O$_3$ (CAS Number 1344-28-1), SiO$_2$(AEROSIL$^®$ 200), SiO$_2$/Al$_2$O$_3$ (MCM41, CAS Number 1318-02-1), SiO$_2$/TiO$_2$ (CAS Number 641731-10G), NaY zeolite (CAS Number 334448), CeO$_2$/ZrO$_2$(CAS Number 53169-24-7), MgSiO$_3$(Florisil, CAS Number 1343-88-0) or α-Al$_2$O$_3$ (CAS Number 234745).

2.2. Characterization

The elemental composition of the samples dissolved in H$_2$SO$_4$/HNO$_3$ was determined by inductively coupled plasma atomic emission spectroscopy (ICP–AES) on a Thermo-Electron 3580 instrument.
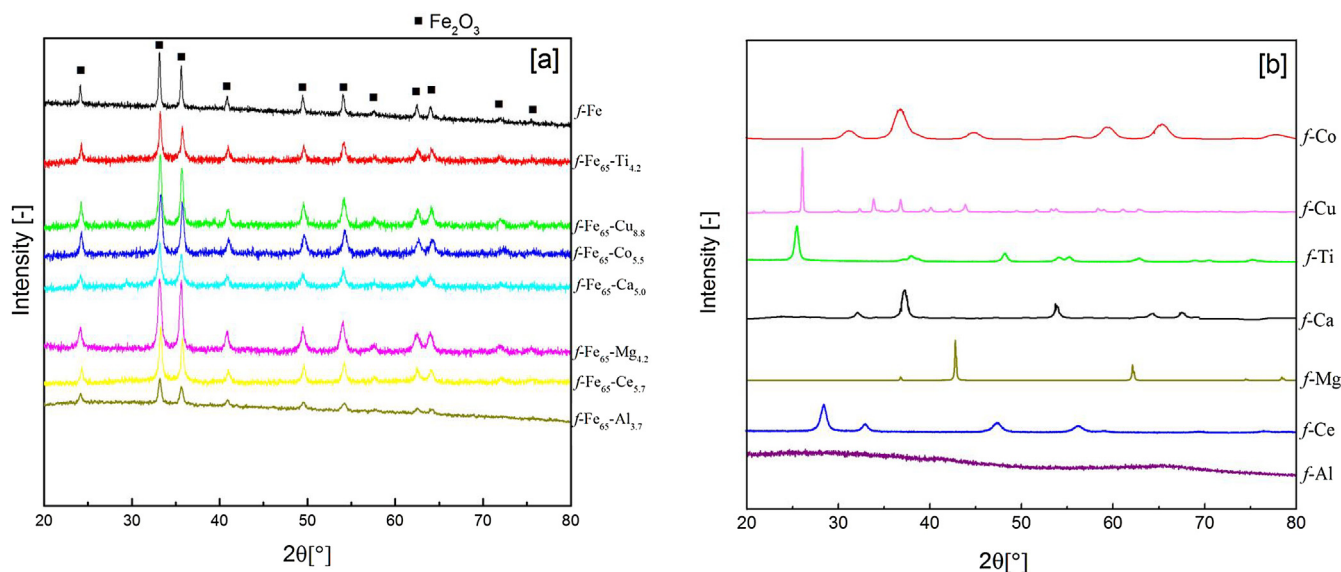
Fig. 1. XRD over prepared samples by fusion method. (a) fused Fe based samples; (b) fused pure additives.

Nitrogen adsorption–desorption isotherms was obtained by a Micromeritrics ASAP-2420 surface area and porosity analyzer instrument. Before the measurement, the samples were degassed in vacuum at 300 °C for 3 h. Specific surface areas and adsorption–desorption isotherms calculated by Brunauer–Emmett–Teller (BET), and Barret–Joyner–Halenda (BJH) method, respectively from the adsorption data.

Both normal and in-situ XRD patterns were collected using a Bruker D8 Advanced A25 diffractometer in Bragg–Brentano geometry fitted with a copper tube operating at 40 kV and 40 mA and a linear position sensitive detector (opening 2.9°). The diffractometer was configured with a 0.36° diverging slit, 2.9° anti scattering slit, 2.5° Soller slits, and a Ni filter. The data sets were acquired in continuous scanning mode (0.008°/s) over the 2θ range 15–120°, using a step interval of 0.04° and a counting time of 5 s per step. The mean crystallite size was calculated using the Scherrer equation.

H_2-TPR (temperature programmed reduction) was performed on an Altamira instrument. The catalyst powder (50 mg) was placed in a U-shaped quartz reactor and pre-treated in flowing Ar (50 mL/min) for 0.5 h at 300 °C, followed by cooling to room temperature. The temperature was then raised from room temperature to 1000 °C at a rate of 10 °C/min under a 5% H_2/Ar flow (50 mL/min). A thermal conductivity detector (TCD) was employed to monitor the H_2 consumption.

The amount of carbon deposited on the catalyst was also analysed using thermos gravimetric analysis (TGA). The spent catalyst powder (20 mg) was placed in an alumina crucible and pre-treated in flowing Ar (50 mL/min) for 0.5 h at 300 °C, followed by cooling to room temperature. The temperature was then raised from room temperature to 1000 °C at a rate of 10 °C/min under air flow (50 mL/min). The sample remained heated at 1000 °C for a period until no weight change was detected. The deposited carbon amount was calculated based on the weight loss.

To estimate the exposed active Fe^0 surface area, H_2 chemisorption on the reduced samples were made at 400 °C and in the pressure range of 10–80 Torr equilibrium pressure range in micromeritics asap 2020 using H_2 as titration reactant [32].

Transmission electron microscopy (TEM) samples were prepared by the conventional method of dispersing a small amount of sample in ethanol and stirring in an ultrasonic bath for 10 min, allowing the homogenized liquid to settle for 5 min and, taking a drop from the top of the vessel to a conventional TEM

holder. The nature of the carbon deposit, size and properties were observed using high-resolution transmission electron microscopy (HRTEM) micrographs obtained from a Titan 60-300 TEM (FEI Co, Netherlands) equipped with an electron emission gun operating at 300 kV. Fast-Fourier transform (FFT) analysis was applied to various regions of the high-resolution TEM micrographs to investigate the crystal structure of various particles.

X-ray absorption spectroscopy (XAS) experiments were performed on the CRG-FAME beamline (BM30B), at the European Synchrotron Radiation Facility in Grenoble. Samples and references (Fe_3C, Fe_3O_4 and Fe_2O_3, and FeO) standards were all diluted with boron nitride (BN) and compressed into a pellet (5 mm diameter) to allow the measurement in transmission mode. For all compounds the dilution level corresponded to the optimal sample thickness for transmission experiments (edge jump close to 1). The spectrum of metallic iron was measured with a metallic foil and was also used to perform the energy calibration of the monochromator (pseudo-channel-cut/Si (220), energy resolution 0.365 eV). The spectra of the iron references are shown in supplementary information. The investigated samples are f-Fe_{65}-$Al_{3.7}$ prepared by fusion method and contacted with a methane flow at 750 °C for x min (x = 2.5, 5, 7.5, 10, 12.5, 15, 20, 25, 60 and 180 min) in a fluidized bed reactor.

All XAS data were analysed using the Demeter package, a graphical interface to the AUTOBK and IFEFFIT code [33]. XANES spectra were obtained after performing standard procedures for pre-edge subtraction, normalization, and polynomial removal. Principal component analysis (PCA) and linear combination method [34], both available in ATHENA, were used to calculate the fraction of various iron phases using the near-edge spectra region between 7120 and 7200 eV. During the activation of the pre-reduction and the catalytic decomposition of methane, PCA identified five major components. The target transform application of the PCA could reconstruct successfully the recorded spectra for Fe, Fe_3C, Fe_3O_4 and FeO references. However, Fe_2O_3 spectrum was rejected by PCA analysis. Linear combination fittings with the four standards identified by PCA were not able to provide complete agreements for the whole series of samples. As the hercynite phase ($FeAl_2O_4$) was evidenced by powder XRD in our previous work with this catalytic system [35], an attempt to reconstruct its spectrum was performed (spectrum provided by the ALS Fe XAS database [36]). A satisfactory agreement was obtained and allowed to identify the fifth missing principal component. Thus, the $FeAl_2O_4$ spectrum
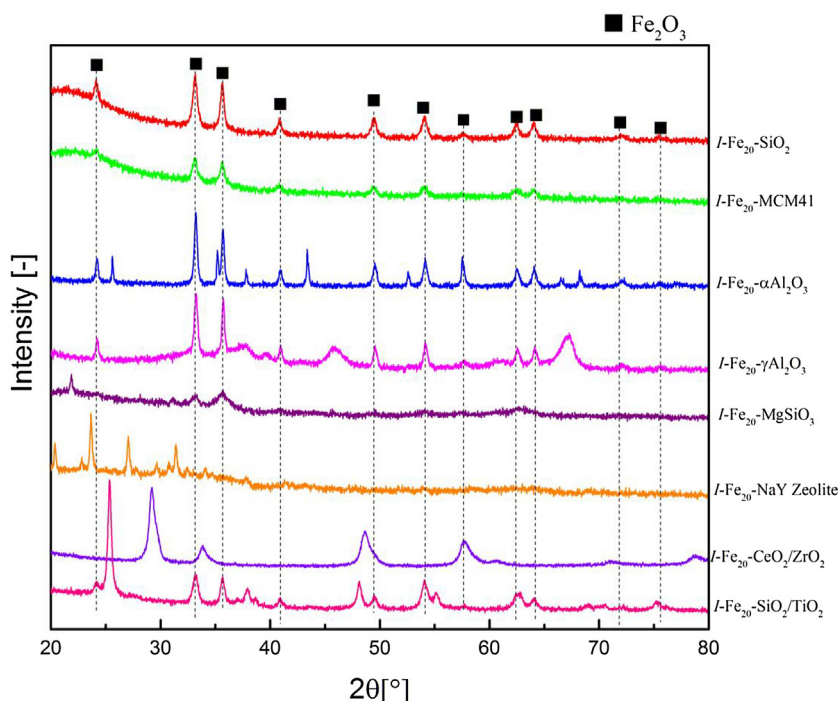
Fig. 2. XRD over prepared samples by impregnation method.

was selected as an additional standard for the linear combination fitting. Parametrization of the fitting included the respective weights of each references spectrum and one additional energy shift parameter for the spectrum of hercynite. The latter parameter was introduced to consider a possible difference between the energy calibration of the spectra recorded at ESRF and the one from ALS database.

2.3. Catalytic evaluation

The CMD performance on the prepared catalysts in this work was conducted in the Microactivity Effi reactor from Process Integral Development Eng & Tech S.L. equipped with a long quartz tube reactor (internal diameter: 10 mm; length: 305 mm). The fine catalysts powders were pelletized into 150–200 μm before loading into the reactor. The reaction temperature was controlled by a thermocouple placed in the center of the catalyst layer. Pure methane was used as the feed for CMD. The loaded catalysts were pre-reduced with pure hydrogen at a selected temperature between 500 and 800 °C. The outlet gases were screened by online gas chromatography (GC; Varian 450) and micro GC (Soprane MicroGC 3000).

3. Results and discussion

3.1. Characterization of fresh catalysts

Regardless of the different additives, XRD patterns over fused Fe-based catalysts in Fig. 1(a), almost show only characteristic peaks of hematite (Fe_2O_3), at 2θ = 24.3°, 33.4°, 35.8°, 41.2°, 49.8°, 54.5°, 58.1°, 62.3°, 64.4°, 72.6° and 75.9°. The position of these diffractions peaks are fitting well with the corresponding (012), (104), (110), (113), (024), (116), (018), (214), (300), (1010) and (220) diffraction planes of hematite α-Fe_2O_3 (PDF Number 33-0664) [37]. The absence of additives reflection peaks can be considered as resulting from these three factors: (1) these additives are amorphous over fused samples; (2) Fe_2O_3 forms solid solution with these additives oxides with the structure of hematite; (3) additives forms very fine oxides par-

ticles beyond the detection limit of XRD. The fused pure additives XRD tests were also done in Fig. 1(b) as references. The results show the characteristic peaks of additives corresponding oxides, which denies their amorphous state assumption over fused samples in Fig. 1(a). The formation of Fe based oxide solid solution has been reported to depend on the preparation method, particularly on the final calcination temperature. C. Laurent et al. [38] prepared Al-Fe-oxides solid solution by calcining at temperatures between 1025 and 1100 °C. The Mg-Fe-oxides solid solution was synthesized by calcination at 732 °C in air from Yoo et al. [39]. Peltekov and Boyanov [40] reported the formation of Ca-Fe-oxides solid solution by calcining at 900–1200 °C. The formation of Ti-Fe-oxides solid solution was proved by Charilaou et al. [41] to be impossible when calcination temperature was lower than 827 °C. The formation of Ce-Fe-Oxides solid solution was found over samples calcined at temperature ranging from 600 to 900 °C by Li et al. [42]. Better defined Co-Fe-oxides solid solution was synthesized by Rives et al. [43] upon calcination at temperature higher than 748 °C. Hirunsit and Faungnawakij [44] developed Cu-Fe-oxides solid solution by calcination at 900 °C.

All these reports suggest that a calcination temperature much higher than 450 °C is required for the formation of solid solutions between Fe and some additives oxides. Therefore, based on above discussion, meanwhile considering the rather lower loading of the additives compared to Fe, the absence of additives reflection XRD peaks in Fig. 1(a) probably results from the high dispersion of fine additives oxides particles over Fe_2O_3 surface. However, we cannot deny the existence of strong interaction between Fe_2O_3 with these additives oxide, which will be discussed in detail in the H_2-TPR discussion. On the other hand, for all the impregnated samples in Fig. 2, the peaks belong to their corresponding supports can be clearly seen. Because of the low calcination temperature (450 °C), no solid solution or spinel reflections can be directly evidenced from the XRD profiles. Further, Fe_2O_3 reflection peaks can be detected for all samples except zeolite and CeO_2/ZrO_2 supported samples. Li et al. [45] assumed that, incorporation of Fe^{3+} (with small ion radius 0.06 nm) into CeO_2/ZrO_2 lattice (with big ion radius Ce^{4+} 0.097 nm,
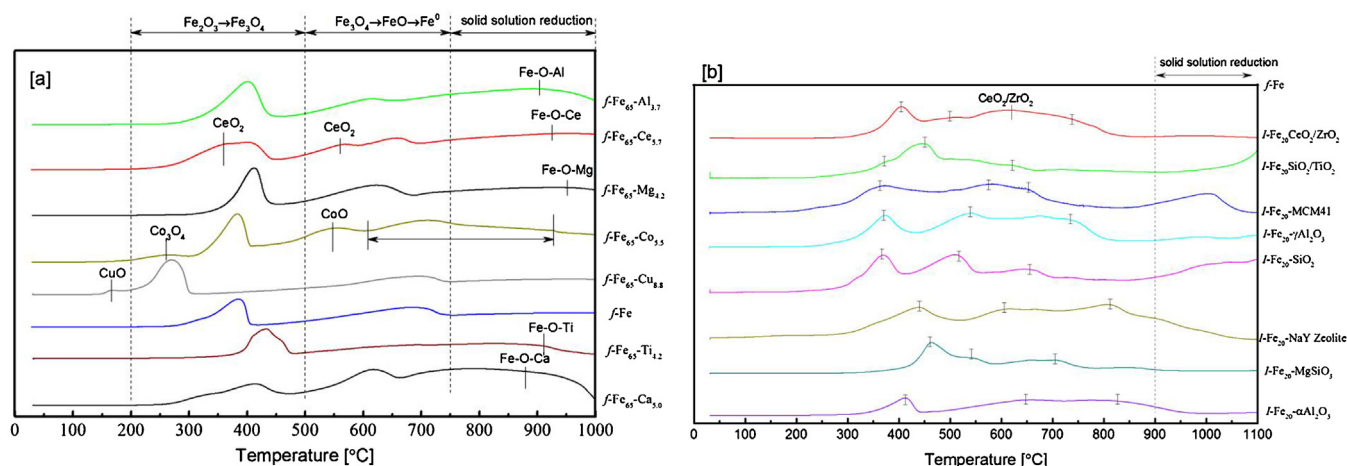
Fig. 3. H$_2$-TPR of prepared samples. (a) fused; (b) impregnated.

Table 2
Characterization of prepared samples.

Catalyst	BET surface area [m^2/g]	Pore volume [cc/g]	Pore size [nm]	Fe oxides crystal size [nm][a]	Fe^0 crystal size [nm][a,b]	H$_2$ uptake [μmol/g$_{cat}$][b]	Fe loading [wt%]
f-Fe$_{65}$-Al$_{3.7}$	57.49	0.20	11.77	19	50	11.08	64
f-Fe$_{65}$-Mg$_{4.2}$	29.88	0.12	11.36	20	76	7.64	66
f-Fe$_{65}$-Ca$_{5.0}$	53.23	0.16	10.51	27	110	4.92	65
f-Fe$_{65}$-Ce$_{5.7}$	54.09	0.19	11.94	25	69	8.23	66
f-Fe$_{65}$-Cu$_{8.8}$	20.97	0.12	15.90	25	92	6.21	65
f-Fe$_{65}$-Co$_{5.5}$	21.08	0.11	17.79	21	87	6.40	65
f-Fe$_{65}$-Ti$_{4.2}$	68.33	0.22	12.04	37	103	5.56	63
f-Fe	11.03	0.10	38.04	56	91	6.01	70
I-Fe$_{20}$-αAl$_2$O$_3$	14.37	0.09	22.20	32	–	–	21
I-Fe$_{20}$-γAl$_2$O$_3$	59.71	0.24	14.72	27	–	–	18
I-Fe$_{20}$-SiO$_2$	163.69	1.13	27.80	19	–	–	19
I-Fe$_{20}$-MCM41	460.09	1.59	12.96	20	–	–	20
I-Fe$_{20}$-SiO$_2$/TiO$_2$	54.01	0.29	21.48	16	–	–	20
I-Fe$_{20}$-NaY Zeolite	180.60	0.07	4.67	–	–	–	21
I-Fe$_{20}$-CeO$_2$/ZrO$_2$	49.83	0.12	7.45	–	–	–	20
I-Fe$_{20}$-MgSiO$_3$	101.76	0.26	13.88	18	–	–	18

[a] Crystallite size was calculated by Scherrer equation.
[b] Sample was reduced by H$_2$ at 750 °C for 1 h.

Zr^{4+} 0.084 nm), resulted in the undetectable Fe$_2$O$_3$ peaks. This can be the same reason for zeolite supported Fe sample, where the Fe may be encapsulated in the NaY zeolite cages [46].

The average Fe$_2$O$_3$ crystallite size over prepared fresh samples and Fe^0 size over H$_2$ 750 °C reduced samples shown in Table 2 were calculated by using Scherrer equation from XRD profiles in Figs. 1 and S1, respectively. For the prepared fresh samples, the pure Fe sample (f-Fe) shows the biggest Fe$_2$O$_3$ particle size of 56 nm, while both fusing and impregnating these Fe$_2$O$_3$ with additives help to disperse them into smaller size of 16–37 nm. Similarly, due to the additives function acting like the support to disperse Fe$_2$O$_3$, both fused and impregnated samples exhibit much larger BET surface area and pore volume while smaller pore size than those of f-Fe sample. Due to the different reducibility and metal support interaction strength, there was a mismatch between Fe$_2$O$_3$ and Fe^0 crystallite size. After 750 °C H$_2$ reduction for 1 h, the exposed Fe^0 active surface area was measured in term of H$_2$ uptake amount, which followed the sequence of f-Fe$_{65}$-Ca$_{5.0}$ < f-Fe$_{65}$-Ti$_{4.2}$ < f-Fe < f-Fe$_{65}$-Cu$_{8.8}$ < f-Fe$_{65}$-Co$_{5.5}$ < f-Fe$_{65}$-Mg$_{4.2}$ < f-Fe$_{65}$-Ce$_{5.7}$ < f-Fe$_{65}$-Al$_{3.7}$. The H$_2$ uptake amount corresponded well with the Fe^0 crystallite size.

In order to understand the redox properties over prepared samples, H$_2$-TPR was conducted in Fig. 3 on both fused and impregnated samples. In Fig. 3(a), pure Fe sample f-Fe shows typical reduc-

tion peaks belong to Fe$_2$O$_3$ [47]. The sharp peak between 300 and 500 °C is normally ascribed to the reduction of Fe$_2$O$_3$ into Fe$_3$O$_4$. Further reducing Fe$_3$O$_4 \rightarrow$ FeO $\rightarrow$ Fe^0 can explain the broad peak appearance at the temperature ranged from 500 to 750 °C. For the f-Fe$_{65}$-Cu$_{8.8}$, the peak at 100–200 °C belongs to CuO reduction. It can be found that the Fe$_2$O$_3 \rightarrow$ Fe$_3$O$_4$ reduction peak shifts from 300 to 500 °C over f-Fe to lower temperature ranged from 200 to 300 °C. The reduced Cu^0 nanoparticles are well known as hydrogen activation sites to spill over H$_2$ [48], which can thus facilitate Fe$_2$O$_3$ reduction to Fe$_3$O$_4$ at low temperature. The reduction of Fe$_3$O$_4 \rightarrow$ FeO $\rightarrow$ Fe^0 seems to be not affected by Cu adding, which gives the same H$_2$-TPR profiles as that of f-Fe. Two extra Co-oxides reduction peaks at 260 °C (Co$_3$O$_4 \rightarrow$ CoO) and 550 °C (CoO $\rightarrow$ Co) [49] can be evidenced over f-Fe$_{65}$-Co$_{5.5}$. The Co addition doesn't change the Fe$_2$O$_3 \rightarrow$ Fe$_3$O$_4$, but broads the Fe$_3$O$_4 \rightarrow$ FeO $\rightarrow$ Fe^0, which is probably resulted from the Co-Fe interaction to make Fe-oxides to be more difficult reduced [50]. For f-Fe$_{65}$-Ti$_{4.2}$ sample, besides overlapped peaks in the range of 350–500 °C, no peak can be observed above 500 °C. Similar result was also reported by F.D. Liu et al. over a Fe$_x$TiO$_y$–Ti(SO$_4$)$_2$ sample [51]. The overlapped peaks can be attributed to the progressive reduction of Fe^{3+}-O-Ti (Fe$_2$O$_3$) to Fe$^{2+/3+}$-O-Ti (Fe$_3$O$_4$) to Fe^{2+}-O-Ti(FeO). It looks like the interaction between Fe and Ti species lowers the reduction temperature from Fe^{3+} to Fe^{2+}, but results in a formation of iron
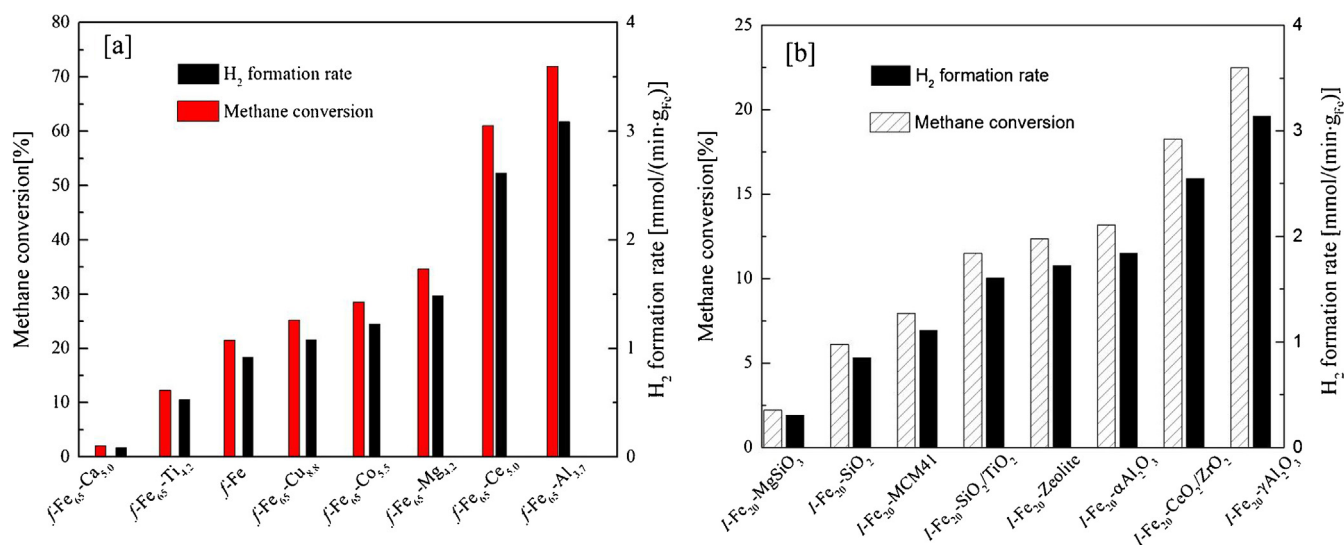
Fig. 4. Initial activity over prepared samples at 750 °C, SV = 1.875 L/g$_{cat}$ h. (a) fused samples; (b) impregnated samples.
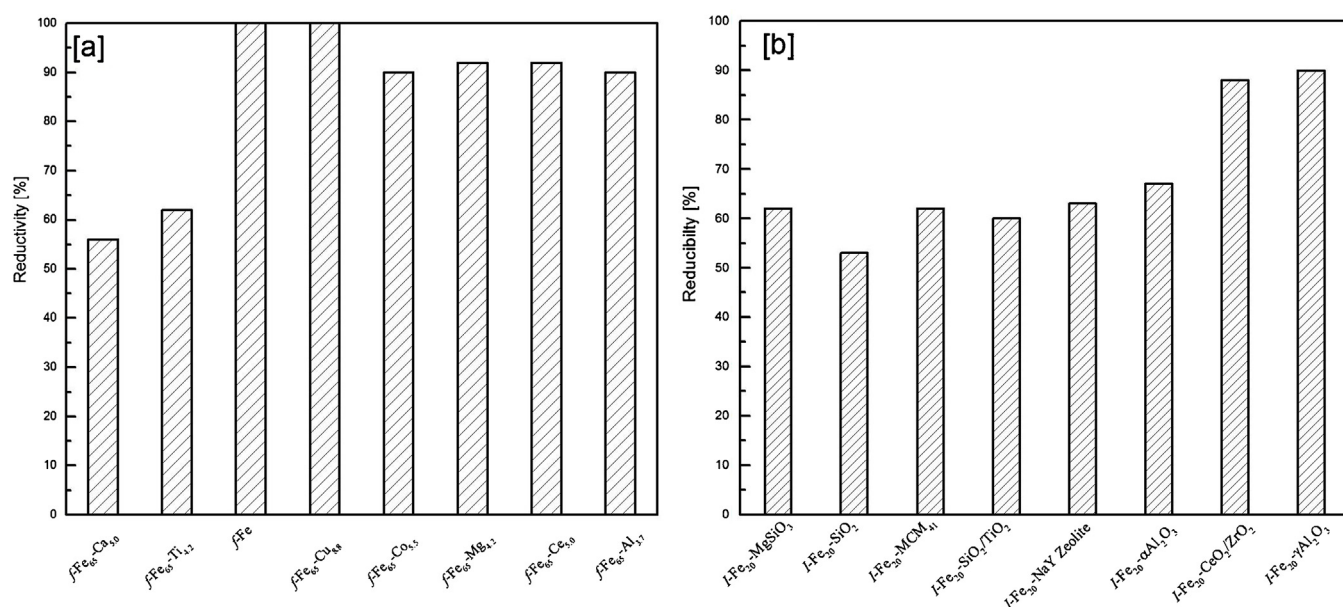

Fig. 5. Samples reducibility at 750 °C H$_2$ measured from H$_2$-TPR profiles in Fig. 4.

titanium phase (Fe^{2+}-O-Ti) which can only be reduced at high temperature of 900–1000 °C. Three reduction zones located at 250–500, 500–750 and 750–1000 °C are shown over f-Fe$_{65}$-Ca$_{5.0}$. The peak at 750–1000 °C is assumed to be the reduction of solid solution Ca-O-Fe [52], although there is no solid solution existence from XRD in Fig. 1(**a**). The reinforcement of Fe-oxide and Ca-oxide interaction during the H$_2$-TPR treatment, especially when the treating temperature is higher than the calcination temperature of 450 °C, may probably result in formation of this solid solution. This is maybe the same reason for the solid solution reduction peaks appearance over f-Fe$_{65}$-Mg$_{4.2}$, f-Fe$_{65}$-Ce$_{5.7}$ and f-Fe$_{65}$-Al$_{3.7}$ samples. Adding Mg or Al or Ce to the f-Fe shifts the Fe$_3$O$_4 \rightarrow$ FeO $\rightarrow$ Fe^0 to a lower temperature by about 50 °C, while little Mg-O-Fe or Fe-O-Al or Ce-O-Fe reduction peak can be detected. The CeO$_2$ reduction peaks can be found at 360 °C and 560 °C [53]. Comparing to fused samples, due to high surface area as well as low Fe loading, impregnated samples must have better Fe dispersion. XRD calculations in Table 2 also show the smaller Fe oxides crystallite size of impregnated than

those of fused samples. The better Fe dispersion thus explains the higher reduction temperature of impregnated samples, meanwhile the separation of overlapped Fe$_3$O$_4 \rightarrow$ FeO $\rightarrow$ Fe^0 broad reduction peaks over fused samples into two peaks over impregnated samples. One additional peak belongs to CeO$_2$-ZrO$_2$ solid solution [54] is detected at c.a. 600 °C for I-Fe$_{20}$-CeO$_2$/ZrO$_2$.

3.2. CMD over prepared Fe catalysts

After pure H$_2$ pre-reduction at 750 °C for 1 h, both fusion and impregnation methods prepared samples are subjected to CMD activity test in Fig. 4. Due to the lower Fe loading, the impregnated samples exhibit worse CMD activity in terms of CH$_4$ conversion ranged from 2 to 25% (Fig. 4(**b**)), than those of fused samples with 2–70% (Fig. 4(**a**)); whereas the activity in term of H$_2$ formation rate over both fused and impregnated samples is almost the same level ranged from 0.3 to 3.2 mmol/(min g$_{Fe}$). The CMD activity of fused samples corresponds well with the H$_2$ uptake amount (i.e.
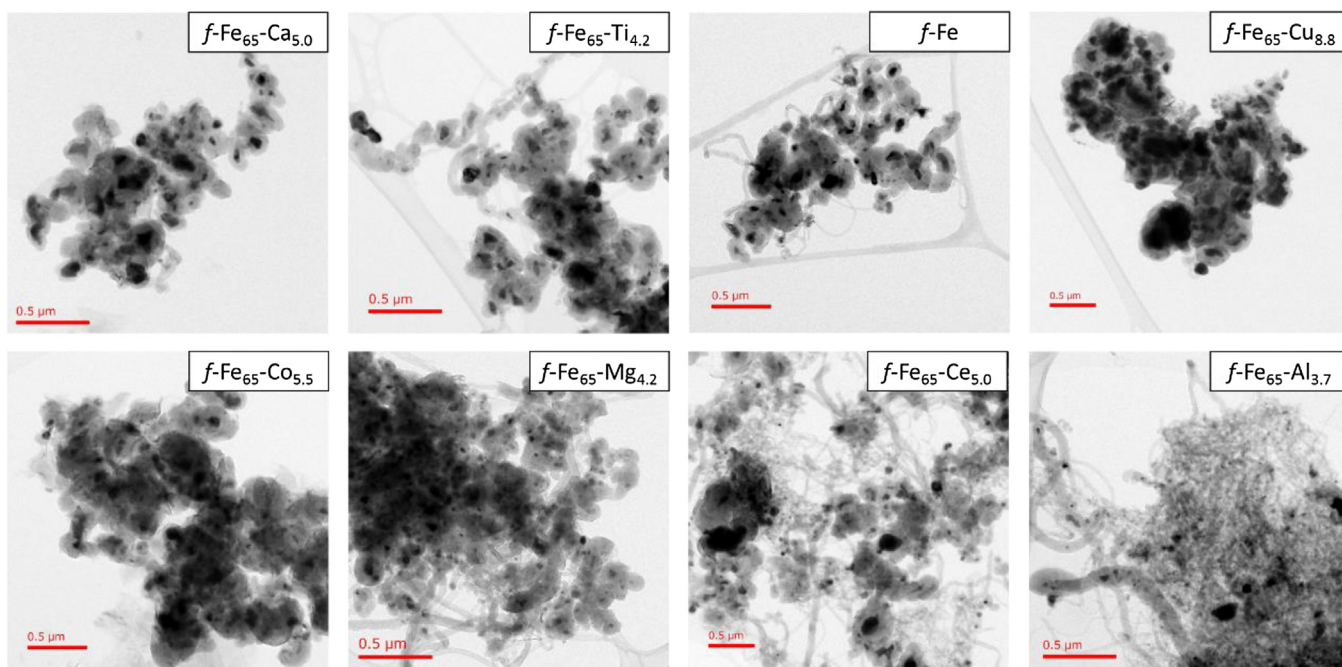
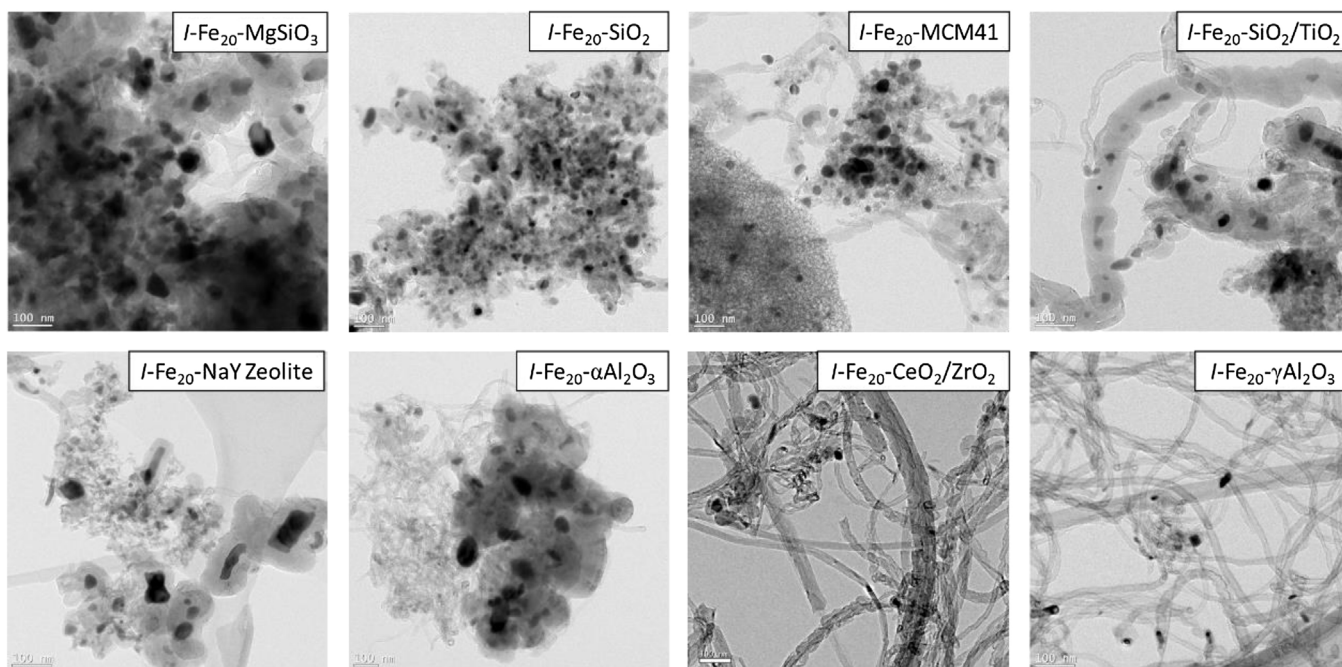**Fig. 6.** TEM images of spent fused samples after CMD at 750 °C for 30 min.

Fig. 7. TEM images of spent impregnated samples after CMD at 750 °C for 30 min.

exposed active Fe^0 surface area), whilst adding Al_2O_3 into Fe catalysts is found to be the best way to improve CMD activity. The Fe^0 surface area after H_2 reduction could be probably affected by reducibility and metal support interaction. Normally, the high reducibility would result in more active Fe^0 surface area. Fig. 5 summarizes the samples reducibility at 750 °C by TPR profiles [55] in Fig. 3. It seems like the catalyst's CMD activity is corresponding with its reducibility for impregnated samples. For fused samples, both f-Fe_{65}-$Ca_{5.0}$ and f-Fe_{65}-$Ti_{4.2}$, show rather bad CH_4 conversions because of their low reducibility ranged between 50 and 60% (due to solid solution formation). The different CMD performance

among fused samples (Cu, Co, Mg, Ce and Al modified Fe catalysts) with same reducibility level (90–100%) further indicated that, besides catalyst's reducibility, some other parameters most probably the different interaction between Fe^0 and support interaction are strongly influencing exposed Fe^0 amount and thus the catalyst's behaviour during CMD.

Kathyayini et al. [56] found iron alone on magnesium salt supports (MgO-Fe) showed much better activity than on calcium salt supports(CaO-Fe). CaO-Fe had 1.7 g_c/g_{cat} carbon deposit, whereas MgO-Fe showed 23.2 g_c/g_{cat}. Fakeeha et al. [57] reported that the H_2 yield was 45% over MgO supported Fe catalyst (30% Fe loading), whereas TiO_2 supported same loading Fe catalyst exhibited only
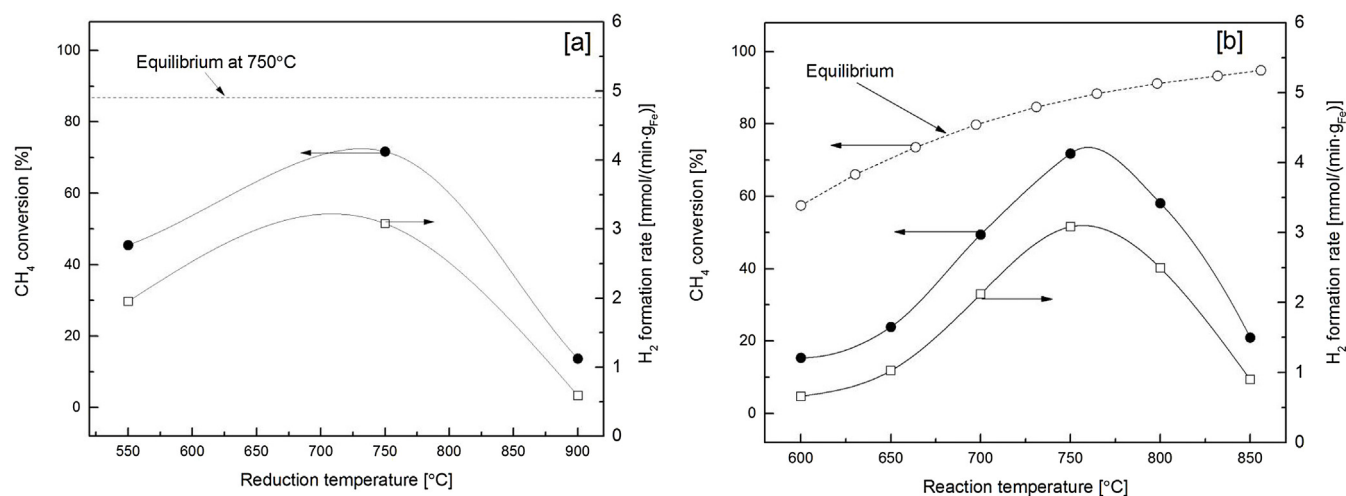
Fig. 8. The effect of reduction and reaction temperature on samples CMD activity at 750 °C, SV = 1.875 L/g$_{cat}$ h.
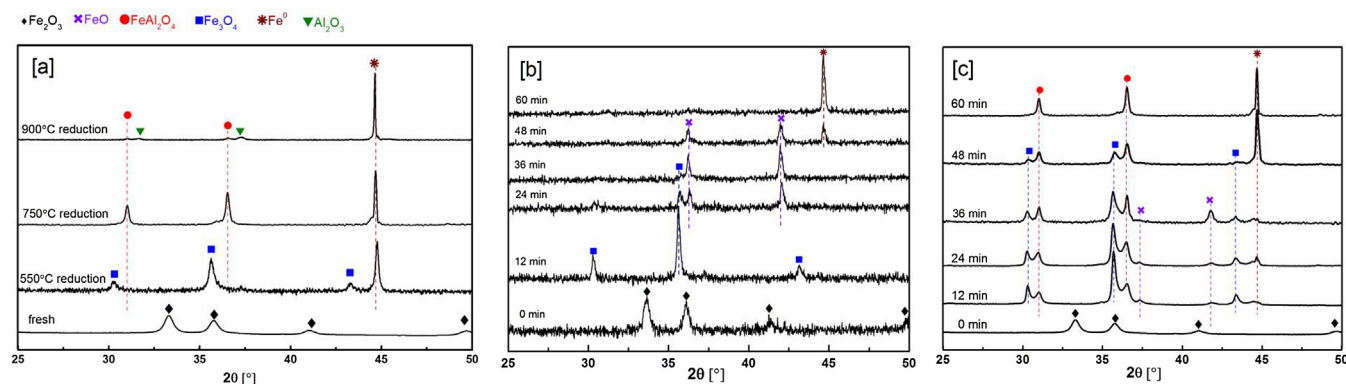

Fig. 9. In-situ XRD reduction mechanism (a) f-Fe$_{65}$-Al$_{3.7}$ with increasing temperature; (b) f-Fe at 750 °C with time on stream; (b) f-Fe$_{65}$-Al$_{3.7}$ at 750 °C with time on stream.

5% H$_2$ yield. Ibrahim et al. [58] investigated the influence of support type in CMD over Fe catalyst, and concluded that Fe/TiO$_2$ was inappropriate for CMD compared to Fe/Al$_2$O$_3$ and Fe/MgO. These results are agreed well with CMD results in Fig. 4(a), where methane conversion decreases with the order of f-Fe$_{65}$-Al$_{3.7}$ (73%) < f-Fe$_{65}$-Mg$_{4.2}$ (34.6%) < f-Fe$_{65}$-Ca$_{5.0}$ (2.1%). Avdeeva et al. [59] reported that the catalyst carbon capacity increased remarkably by adding 6% Co to 50%Fe/Al$_2$O$_3$ from 26.5 to 52.4 g$_c$/g$_{cat}$. Reshetenko et al. [60] attributed the improvement attained with the Fe and Co alloy formation leading to an optimum particle size distribution. Tang et al. [29] compared Fe and Ceria and Fe-Ce bimetallic catalysts CMD activity using a fixed bed reactor at 750 °C. The Ce monometallic catalyst showed very small CH$_4$ conversion activity. Fe catalyst showed 60% CH$_4$ conversion, whereas 77% CH$_4$ conversion was observed by using mixed catalysts 60 wt% Fe$_2$O$_3$–40 wt% CeO$_2$. The improved dispersion of Fe catalyst after adding Ce, together with the continuous oxidation of carbonaceous species by high mobility lattice oxygen in the solid solution (Ce-O-Fe and CeO$_2$/ZrO$_2$), were considered to maintain the active surface area for the reaction. In present study, both f-Fe$_{65}$-Ce$_{5.0}$ and I-Fe$_{20}$-CeO$_2$/ZrO$_2$ also show the positive effect of adding Ce and/or Zr to the Fe catalysts on CMD activity. Although Cu does not chemisorb methane and show no activity for carbon deposition in hydrocarbons reforming, the segregated and/or alloyed Cu would show a significant effect on the coke formation. Fe–Cu Raney-type catalysts were reported by Cunha et al. [30] to show higher CMD stability than the monometallic Raney-Fe catalysts. Takenaka et al. [61] reported the formation rate of H$_2$ during CMD of Fe$_2$O$_3$/SiO$_2$ (20 μmol/min) was significantly lower

than that for Fe$_2$O$_3$/Al$_2$O$_3$ (1100 μmol/min). It is like the interaction of α-Fe with silica supports brings about a decrease in carbon solubility and diffusion rate of carbon atoms in the metal. Li et al. [62] reported a better methane conversion during CMD on Fe/Al$_2$O$_3$ than Fe/zeolite catalysts. By checking the binding energy through X-ray photoelectron spectroscopy (XPS) spectrograms, they suggested lower reducibility (stronger metal-support interaction) of Fe/zeolite than that of Fe/Al$_2$O$_3$ probably resulted in its worse CMD activity.

Figs. 6 and 7 show the TEM morphologies of deposited carbon over both spent fused and impregnated samples after CMD. Obviously, the formation of CNTs rather than CNOs is preferable for CMD [63]. The Fe^0 metal encapsulated inside the CNOs is totally inactivated, whereas the CNTs can anchor some Fe^0 on their tip to maintain the CMD activity. Li et al. [62] reported similar results stating that, Fe^0, which could be dispersed into the pore of zeolite crystallites, may be totally deactivated due to the blockage of pore by carbon deposition during CMD; whereas, Fe^0 particles, those were found to be dispersed on Al$_2$O$_3$ external surface and be anchored on the tip of formed CNTs, could be still available for CMD. In all, it is likely that the nature of the support, the catalyst and most importantly the type of interaction between the metal and the support has a great influence on both CMD activity and deposited carbon morphologies. Among all investigated samples, the Fe-Al$_2$O$_3$ catalysts show the best CMD performance. Perhaps Al$_2$O$_3$ affected Fe crystallization to expose more (111) faces out of the surface area, which are necessary for the deposition of graphitic carbon upon CMD [59]. As explained by our previous study [8], the
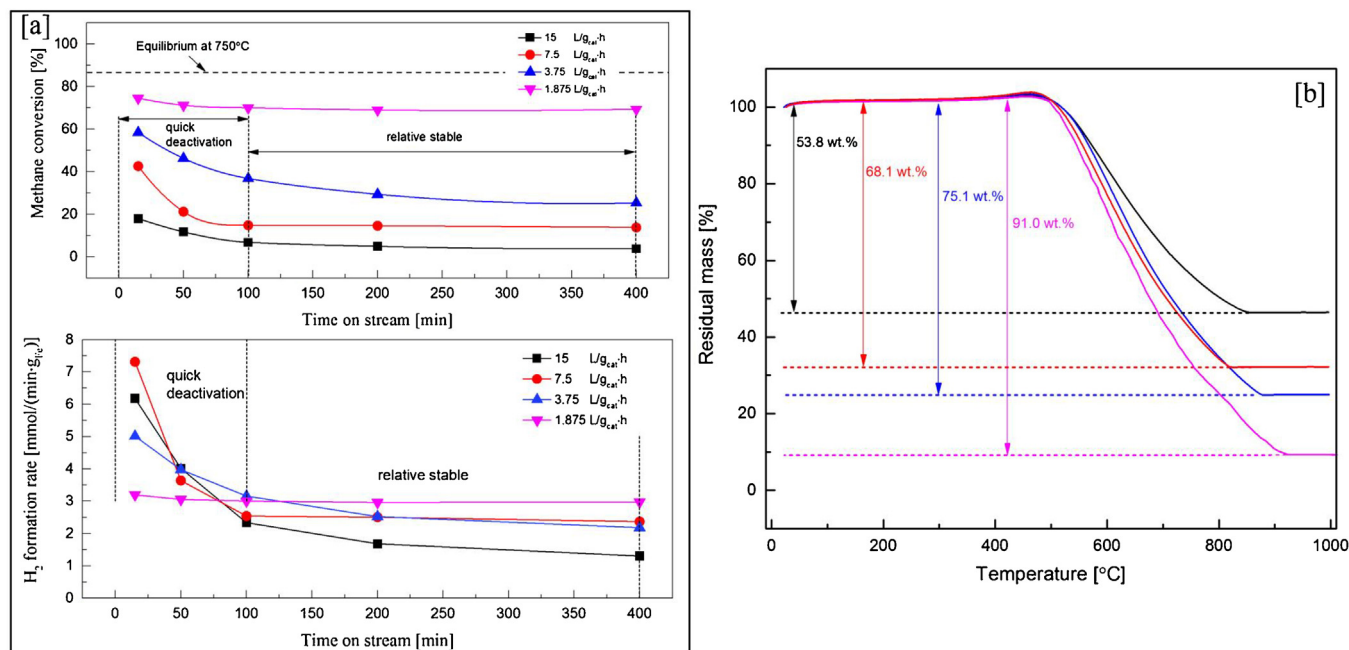
Fig. 10. SV influence on catalysts CMD performance at 750 °C: (a) activity and life test; (b) TGA analyses of carbon deposition.

deposited carbon morphology over Ni catalysts is usually defined by the comparison between CH_4 activation-decomposition rate and its diffusion-graphite formation rate. It looks like the combination of Fe^0 and Al_2O_3 would balance these two rates to continually form CNTs, which will help to maintain high CMD activity.

3.3. Study of f-Fe_{65}-$Al_{3.7}$ for CMD

3.3.1. Activity over f-Fe_{65}-$Al_{3.7}$ for CMD

The sample redox properties under different temperatures are clearly studied in Fig. 3 by H_2-TPR analysis. Here, selecting *f*-Fe_{65}-$Al_{3.7}$ as a representative sample, the influence of both reduction and reaction temperatures on *f*-Fe_{65}-$Al_{3.7}$ CMD activity is investigated in Fig. 8. From Fig. 8(**a**), the catalyst reduced at 750 °C shows the best CMD activity in terms of methane conversion, while the catalyst activated at 900 °C exhibits the lowest methane conversion. Pinailla et al. [28] compared the CMD performance over a FeMo/MgO catalyst under different temperature (550, 700 and 800 °C) reduction. They found the Fe^0 sintered substantially into big aggregates with reduction temperature increase. The sintered Fe^0 thus resulted in the catalyst's worse CMD activity and stability. For the *f*-Fe_{65}-$Al_{3.7}$ in this study in Fig. 9(**a**), we found the sample is composed of Fe^0 (36 nm) and Fe_3O_4 after 550 °C reduction, Fe^0 (50 nm) and $FeAl_2O_4$ after 750 °C reduction. Further raising the reduction temperature from 750 to 900 °C, reduces part of $FeAl_2O_4$ and sinters Fe^0 into big particles of c.a. 143 nm. The sample reducibility, Fe^0 crystallite size and active Fe^0 amount measured by H_2 chemisorption was summarized by **Table S1**. It can be speculated that the interaction between Fe^0 (with an appropriate size) and $FeAl_2O_4$ plays a positive role for the CMD performance. To our knowledge, no literature is found to discuss the effect of $FeAl_2O_4$ formation through CMD activity. $FeAl_2O_4$ itself is of course inactive for CMD, but its existence could help to mitigate the Fe^0 agglomeration through the strong bonding between Fe^0 and $FeAl_2O_4$. Similar mechanism over Ni^0 and $NiAl_2O_4$ has been well accepted in literature [55], which stated that positive effect of $NiAl_2O_4$ was found to strongly anchor the Ni^0 particles on its top against sintering for methane reforming. The strong bonding between Fe^0 and $FeAl_2O_4$ probably can maintain the active Fe^0 amount by hindering the quasi-liquid Fe^0 to be split into smaller

particles and absorbed into the interior of CNTs. CNTs trapped Fe^0 would lose their activity due to the limited contact with CH_4 gas. In Fig. 8(**b**), after reducing with H_2 at 750 °C, *f*-Fe_{65}-$Al_{3.7}$ is subjected to a CMD reaction from 600 to 850 °C. The catalyst's activity increases with temperature until reaches the peak at 750 °C. Further raising temperature higher than 750 °C lowers the catalyst's CMD performance, which could be probably resulted from the Fe^0 and/or Al_2O_3 sintering together with $FeAl_2O_4$ partial reduction to change the interaction between Fe^0 and $FeAl_2O_4$. As shown in Table S1, increasing the reduction temperature would not only increase the catalyst's reducibility, but also increase the Fe^0 crystallite size. The exposed active Fe^0 amount is of course directly related both reducibility and Fe^0 size. The high reducibility and larger crystallite size with little exposed Fe^0 amount would affect the CMD activity in the opposite ways, which explains the existence of an optimized reduction temperature to maintain the highest Fe^0 amount. In all, conducting both pre-reduction with H_2 and CMD reaction at 750 °C is concluded as the optimized reaction condition for *f*-Fe_{65}-$Al_{3.7}$ to obtain a high CMD activity.

In order to understand *f*-Fe_{65}-$Al_{3.7}$ reduction mechanism at 750 °C, an in-situ XRD test with time on stream is investigated in Fig. 9(**b**) and (**c**). For unsupported pure Fe catalyst *f*-Fe (Fig. 9(**b**)), Fe_2O_3 can be seen progressively reduced into Fe^0. After 12 min, all Fe_2O_3 was reduced to Fe_3O_4. This Fe_3O_4 was gradually reduced into FeO until vanished after 36 min. After 60 min, the sample was composed of Fe^0, without any Fe oxides. Therefore, the reduction of *f*-Fe follows the generally accepted stepwise reduction mechanism as $Fe_2O_3 \rightarrow Fe_3O_4 \rightarrow FeO \rightarrow Fe^0$. For *f*-$Fe_{65}$-$Al_{3.7}$, after 12 min, there was no reflection peaks of Fe_2O_3, but showing $FeAl_2O_4$, Fe_3O_4, FeO and Fe^0. With time on stream from 12 to 36 min, $FeAl_2O_4$ and Fe^0 seemed no change, whilst Fe_3O_4 can be seen gradually reduced into FeO, which was totally reduced into Fe^0 after 48 min. After 60 min, all the left Fe_3O_4 were further reduced into Fe^0 while remaining $FeAl_2O_4$, which can only be reduced at a higher temperature than 900 °C from H_2-TPR profile in Fig. 3. Obviously, by adding Al_2O_3, the reduction of Fe oxides becomes complicated due to the interaction between Fe and Al_2O_3 to form $FeAl_2O_4$. But still the progressive $Fe_2O_3 \rightarrow Fe_3O_4 \rightarrow FeO \rightarrow Fe^0$ can be somehow seen from the in-situ XRD results. The formation of
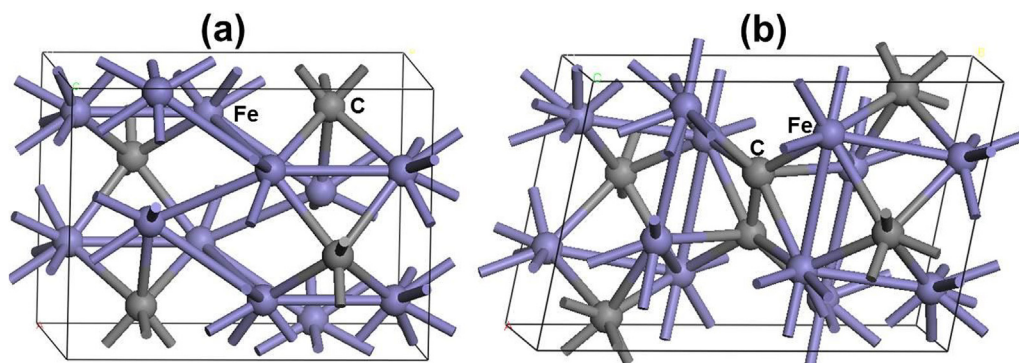
Fig. 11. DFT-optimized lowest-energy structures of (a) Fe_3C and (b) $Fe_3C_{1.5}$. Color legend: Fe in purple and C in gray.

$FeAl_2O_4$ is considered to result from our previous reported reaction [31] as $Fe_3O_4 + Fe^0 + 4Al_2O_3 \rightarrow 4FeAl_2O_4$; $FeO + Al_2O_3 \rightarrow FeAl_2O_4$ or $Fe_3O_4 + H_2 + 3Al_2O_3 \rightarrow 3FeAl_2O_4 + H_2O$.
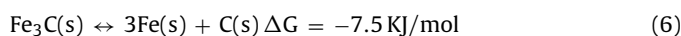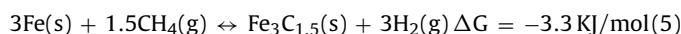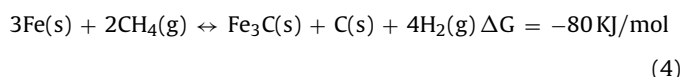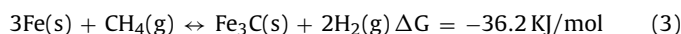
The influence of space velocity (SV) on f-Fe_{65}-$Al_{3.7}$ CMD performance at 750 °C in terms of methane conversion, H_2 formation rate, life time and carbon deposition amount is investigated in Fig. 10. The catalyst is pre-reduced by H_2 at 750 °C for 1 h. As shown in Fig. 10(a), at a low SV of 1.875 L/g_{cat} h, except slight deactivation during the first 100 min, the sample shows a stable methane conversion (c.a. 70%) and H_2 formation rate (3.2 mmol/(min g_{Fe})) for 400 min. However, doubling the SV from 1.875 to 3.75 L/g_{cat} h by increasing the flow rate but keeping the loaded catalysts weight, the sample initial methane conversion decreases from 70% to 60%, whilst the H_2 formation rate was increased from 3.2 to 5.0 mmol/(min g_{Fe}). Further, at SV of 3.75 L/g_{cat} h, the sample is found to show CMD performance as two different stages, i.e., the sample deactivates very quickly from 60% of methane conversion (5.0 mmol/(min g_{Fe}) of H_2 formation rate) at initial to c.a. 40% (3.2 mmol/(min g_{Fe}) of H_2 formation rate) at 100 min; after 100 min, the sample enters into a relatively stable period and finally shows c.a. 25% methane conversion (2.2 mmol/(min g_{Fe}) of H_2 formation rate) at 400 min. Similar results are observed when conducting the CMD at a higher SV of 7.5 and 15 L/g_{cat} h. It is clear, the initial methane conversion and stability of f-Fe_{65}-$Al_{3.7}$ during CMD decrease substantially when the SV increases. However, the initial activity in term of H_2 formation rate seems to reach a plateau at SV = 7.5 L/g_{cat} h. As shown in Fig. 10(b), the spent samples in Fig. 10(a) are subjected to TGA analyses from room temperature to 1000 °C under air atmosphere. The weight loss is resulted from the deposited carbon combustion during the temperature ranged from c.a. 500 to 900 °C. Corresponding to methane conversion and stability change, the carbon deposition amount also decreases with SV increment in the range of 1.875–15 L/g_{cat} h.

3.3.2. CMD mechanism over Fe catalysts

According to our previous research [8,31,35,63], CMD reaction mechanism is found to be totally different between Ni and Fe-based catalysts. Three steps are to occur assumed during the MCD reaction over Ni-based catalysts: CH_4 activation-decomposition on the Ni particle to produce H_2 and carbon, carbon diffusion through the bulk of Ni particle and carbon precipitation. For Fe-based CMD reaction, the model of carbon deposit on Fe_3C is well agreed among researchers [28,35,64,65]. By monitoring a CMD reaction over a fused Fe-Al catalyst by in-situ XRD in our previous study [35], it was found that, substantial amount of Fe_3C accompanied with few graphite carbon (weight concentration ratio of Fe_3C/C is c.a. 87/13) formed after starting CMD reaction over activated fused Fe-Al catalyst for just 2.5 min. After that, the Fe_3C concentration kept stable while graphite concentration increased gradually with time on stream. These results clearly indicated that the formation

of graphite carbon came after that of Fe_3C. It is widely accepted that Fe_3C plays a key role for the CNTs formation during CMD process. Zaiakovskij et al. [66] concluded a Fe_3C cycle mechanism for the formation of CNTs during 1,3-Butadiene cracking on Fe/Al_2O_3 Catalysts. Schaper et al. [67] proposed the concept of CNTs formation via an intermediate Fe_3C phase, i.e., dissolution of carbon in the metal catalyst and of the carbon-through-metal diffusion.

A density functional theory (DFT) study was conducted here to further understand the reaction mechanism over Fe catalysts for CMD. The Gibbs free energy (ΔG) of the various possible obtained solid products from CMD over Fe catalysts at 750 °C under atmospheric pressure, such as perfect or over-stoichiometric iron carbide (Fe_3C, or Fe_3C_{1+x} while it is simplified as $Fe_3C_{1.5}$ in this study) and graphite (C) was investigated by DFT while considering the three chemical reactions (Eqs. (3)–(5)). The possible decompositions of iron carbide (Fe_3C and $Fe_3C_{1.5}$) into Fe^0 and C were also investigated using the two chemical reactions (Eqs. (6) and (7)). More detailed information about the computational methodology used here is described in the Supporting Information.

$$3Fe(s) + CH_4(g) \leftrightarrow Fe_3C(s) + 2H_2(g) \quad \Delta G = -36.2 \, KJ/mol \qquad (3)$$

$$3Fe(s) + 2CH_4(g) \leftrightarrow Fe_3C(s) + C(s) + 4H_2(g) \quad \Delta G = -80 \, KJ/mol \qquad (4)$$

$$3Fe(s) + 1.5CH_4(g) \leftrightarrow Fe_3C_{1.5}(s) + 3H_2(g) \quad \Delta G = -3.3 \, KJ/mol \qquad (5)$$

$$Fe_3C(s) \leftrightarrow 3Fe(s) + C(s) \quad \Delta G = -7.5 \, KJ/mol \qquad (6)$$

$$Fe_3C_{1.5}(s) \leftrightarrow Fe_3C(s) + 0.5C(s) \quad \Delta G = -54.8 \, KJ/mol \qquad (7)$$
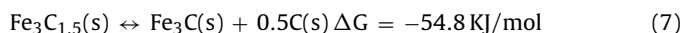
Several structural configurations for $Fe_3C_{1.5}$ were performed by inserting two extra C atoms at various positions into the orthorhombic unit cell of Fe_3C (space group is PNMA), which contains 4 functional units ($Fe_{12}C_4$). The crystal structures were optimized using the spin-polarized periodic DFT implemented in the Vienna Ab-initio Simulation Package (VASP) program [68,69] with the Perdew-Burke-Emzerhof (PBE) exchange-correlation functional [70] and the Projector-Augmented Plane Wave (PAW) approach [71]. The Brillouin zones for Fe_3C and $Fe_3C_{1.5}$ were sampled with a $6 \times 4 \times 6$ Monkhorst-Pack k-point grid while that for cubic Fe was sampled with a $7 \times 7 \times 7$ k-point mesh [72]. The DFT-optimized crystal structure for Fe_3C and the most stable one obtained for $Fe_3C_{1.5}$ are displayed in Fig. 11. For Fe_3C, the calculated lattice constants (a = 5.03 Å, b = 6.70 Å, c = 4.47 Å and $\alpha = \beta = \gamma = 90°$) were found to be in good agreement with the experimental data with Fe-C bond lengths ranging from 1.96 to 2.0 Å and Fe–Fe bond lengths ranging from 2.44 to 2.57 Å (see Fig. 1a). For $Fe_3C_{1.5}$, the lowest-energy structure was obtained when a carbon dimer
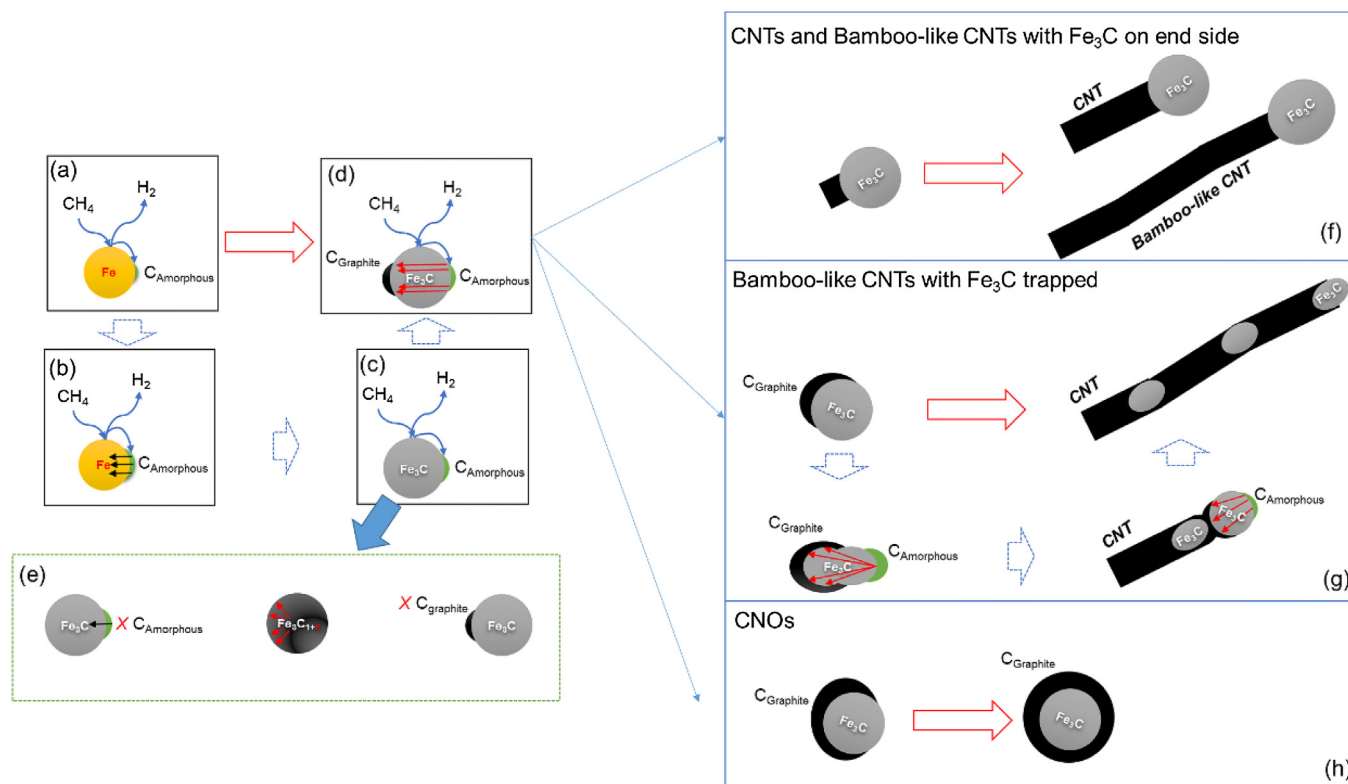
Fig. 12. CMD mechanism models over Fe catalysts.

with a C—C bond length of 1.52 Å. It exhibits a triclinic crystal lattice (symmetry group is P_1) with calculated lattice lengths of a = 4.92 Å, b = 7.36 Å and c = 4.69 Å and angles of α = 84.6°, β = 88.7° and γ = 101.6°. The various bond lengths in this structure were found to be varying from 1.91 to 2.07 Å for Fe-C and from 2.37 to 2.59 Å for Fe–Fe (see Fig. 1b).

The calculated Gibbs free energy of Reaction (4) releasing Fe_3C and C materials together was found to be −80.0 KJ/mol, while those of Reactions (3) and (5) giving either Fe_3C or $Fe_3C_{1.5}$ are found to be −36.2 and −3.3 kJ/mol, respectively. Moreover, the calculated Gibbs free energy of Reaction (6) associated with the decomposition of Fe_3C into Fe^0 and C was found to be −7.5 kJ/mol, whereas that for Reaction (7) associated with the possible decomposition of $Fe_3C_{1.5}$ into Fe_3C and C was found to be −54.8 kJ/mol. As the obtained Gibbs free energy of Reaction (4) is much lower than other reactions, it can be clearly concluded that CMD over Fe catalysts is thermodynamically favourable to ultimately produce Fe_3C together with C. On the second hand, although the calculated Gibbs free energy of Reaction (6) is much higher than that of Reaction (4), it is still slightly exothermic, which means Fe^0 could be possibly decomposed from Fe_3C in a very low probability. Interestingly, the calculated Gibbs free energy of Reaction (7) is much lower than that obtained for Reaction (5). As a conclusion, the decomposition of $Fe_3C_{1.5}$ into Fe_3C and C is a thermodynamically much more favoured process than the formation of $Fe_3C_{1.5}$. Or in other words, even if $Fe_3C_{1.5}$ is formed during the CMD, it will be immediately decomposed to Fe_3C and C.

Based on the DFT and experimental observations discussed above, the Fe_3C formation and its role for the carbon deposition during the CMD is further illustrated in Fig. 12(a–e). In the first stage, CH_4 decomposes to H_2 and amorphous carbon at the Fe^0 surface shown in Fig. 12(a). It is reported that, due to the bcc crystal lattice of Fe^0, whose interstitial position configuration and dimension

do not allow easy accommodation of C atoms, carbon solubility in Fe^0 is as low as below 0.022 wt% in Fe^0 [73]. Thus, according to the Fe-C diagram state reported by C.T. Wirth et al. [74], when the deposited carbon amount exceeds this carbon solubility limitation, as illustrated in Fig. 12(b)(c), the formation of Fe_3C occurs by the rearrangement of iron atoms [64]. Furthermore, Fe_3C structure is quite stable and its decomposition requires a long enough period at a higher temperature than 750 °C. R. Sharma et al. [75] also suggested that decomposition of Fe_3C is not necessary for CNT nucleation and growth as the enclosed particles after the growth retain cementite structure.

As Fe_3C is also a catalyst for CMD [74,75], methane continues its decomposition on the Fe_3C surface. The continues deposition of carbon would result in the over saturation of Fe_3C to form Fe_3C_{1+x} shown in Fig. 12(e), which may further decompose to Fe_3C and graphite carbon on one of the crystallographic areas of Fe_3C. R. Sharma et al. [75] found that the time interval between formation of Fe_3C and the spurt of graphite carbon (CNTs) is as short as less than a second (0.11 s). Therefore, it is easily to be confused that the graphite is directly deposited on the Fe_3C surface. However, here in this study, based on the DFT study, we believe the supersaturated Fe_3C decomposition probably precipitate the amorphous carbon arising out of methane cracking to graphitic one (Fig. 12(d)). A total reaction mechanism is summarized in following equations (Eqs. (8)–(11)). CMD is supposed to be initialized on the Fe^0 surface to decompose CH_4 into amorphous carbon and H_2. The amorphous carbon will soon react with Fe^0 to form Fe_3C or mixture of Fe^0 and Fe_3C, which will continue to play as the catalyst to decompose CH_4. The formed carbon will diffuse into Fe_3C to form supersaturated cementite, which will immediately decompose back to stoichiometric Fe_3C and meanwhile "transfer" amorphous carbon to graphite carbon. Further, due to the partial coverage of Fe^0/Fe_3C by the deposited graphite, the catalyst would
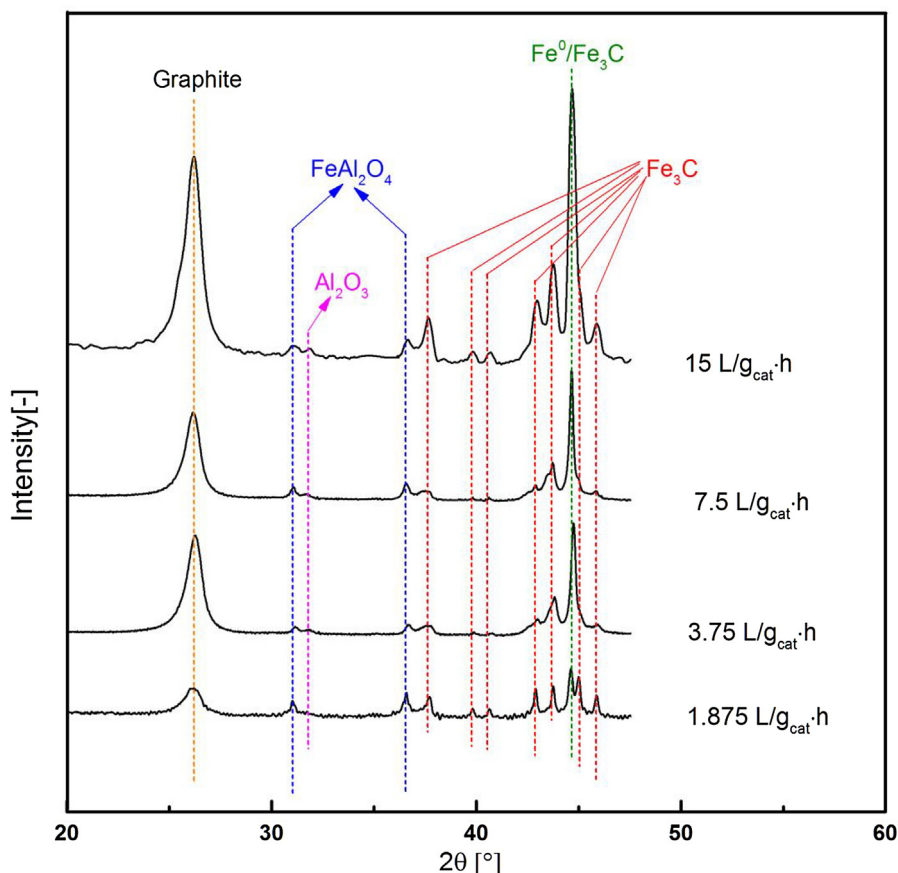
Fig. 13. XRD over spent catalysts tested at Fig. 10(a) with different SV.

lose some of its activated exposed surface and thus show a quick deactivation, which is corresponding to the CMD performance during the first 100 min as shown in Fig. 10(**a**).

$$CH_4 \overset{Fe^0}{\leftrightarrow} C_{amorphous} + 2H_2 \tag{8}$$

$$Fe^0 + C_{amorphous} \leftrightarrow Fe_3C \tag{9}$$

$$CH_4 \overset{Fe_3C/Fe^0}{\leftrightarrow} C_{amorphous} + 2H_2 \tag{10}$$

$$C_{amorphous} \overset{Fe_3C}{\leftrightarrow} C_{graphite} \tag{11}$$

By the DFT results, the simultaneous formation of Fe_3C and C during CMD would be the most expected reaction, which is in excellent agreement with the XRD observations over spent catalysts in Fig. 10(**a**) shown in Fig. 13. Regardless of the SV, all spent catalysts showed the Fe_3C reflection peaks together with that of graphite C. The existence of metallic Fe^0 are also confirmed. According to Wrobel et al. [64], the graphite encapsulated Fe_3C is inactive for CMD and Fe_3C itself is going to further decompose into Fe^0 and C, which is a possible reaction indicated by our DFT study. The intensity of graphite diffraction peaks agrees well with the coking amount measured by TGA.

In our previous study [35], methane gas, instead of H_2, was reported to be capable of activating f-Fe_{65}-$Al_{3.7}$ for CMD reaction at 750 °C. Herein, in order to understand the catalyst's structure change during CMD, the ex-situ X-ray absorption near-edge spectra (XANES) at Fe K-edge for the catalyst f-Fe_{65}-$Al_{3.7}$ contacted with pure methane flow at 750 °C with different duration are conducted shown on Fig. 14(**a**). Between 2.5 and 7.5 min, a weak peak in the pre-edge region due to the $1s \rightarrow 3d$-$4p$ transitions and an intense white line due to $1s \rightarrow 4p$ dipolar transition revealed an

oxidized state of iron [76,77]. After 10 min of contact with pure methane at 7.5 L/g_{cat} h, the XANES spectra depicted a noticeable increases of the pre-edge peak and a strong decreases of the white line intensity. The main absorption edge energy, defined at the first inflection point, appeared to be continually shifted to lower energy. Both observation pointed to a progressive reduction of the catalyst occurring with longer duration under CH_4 flow. A more quantitative assessment of the phase transformation taking place is shown in Fig. 14(**b**), which presents the relative abundances of the various phases required to describe the experimental near-edge spectra. During the first 10 min, f-Fe_{65}-$Al_{3.7}$ is composed of a complex mixture of Fe_3O_4, FeO, and $FeAl_2O_4$ oxides. Their absolute proportion rapidly decreased starting from 7.5 min while Fe_3C and metallic Fe were formed quantitatively. Thus, the first 10 min of reaction defined the activation stage of the catalyst. Furthermore, after 60 min of catalytic methane decomposition, f-Fe_{65}-$Al_{3.7}$ was found to be a mixture of Fe^0 and Fe_3C with a little $FeAl_2O_4$. The amount of calculated Fe_3C is almost four times higher than that of Fe^0 phase, which indicates Fe_3C is prefer to form upon reacting methane with Fe^0. A more accurate amount calculation of all possible phases over f-Fe_{65}-$Al_{3.7}$ during CH_4 activated CMD was conducted based on ex-situ XRD and TGA (see supplementary information) [35]. According to Fig. S2, the amount of Fe^0 and Fe_3C is almost stable during 12–25 min, whereas significant increment of carbon proportion can be seen. This corresponds well to the mechanism proposed in Fig. 12, indicating that carbon is not originating from Fe_3C decomposition. The lowering of Fe_3C concentration accompany with slightly increment of Fe^0 amount after 25 min, may probably result from the decomposition of graphite encapsulated Fe_3C.
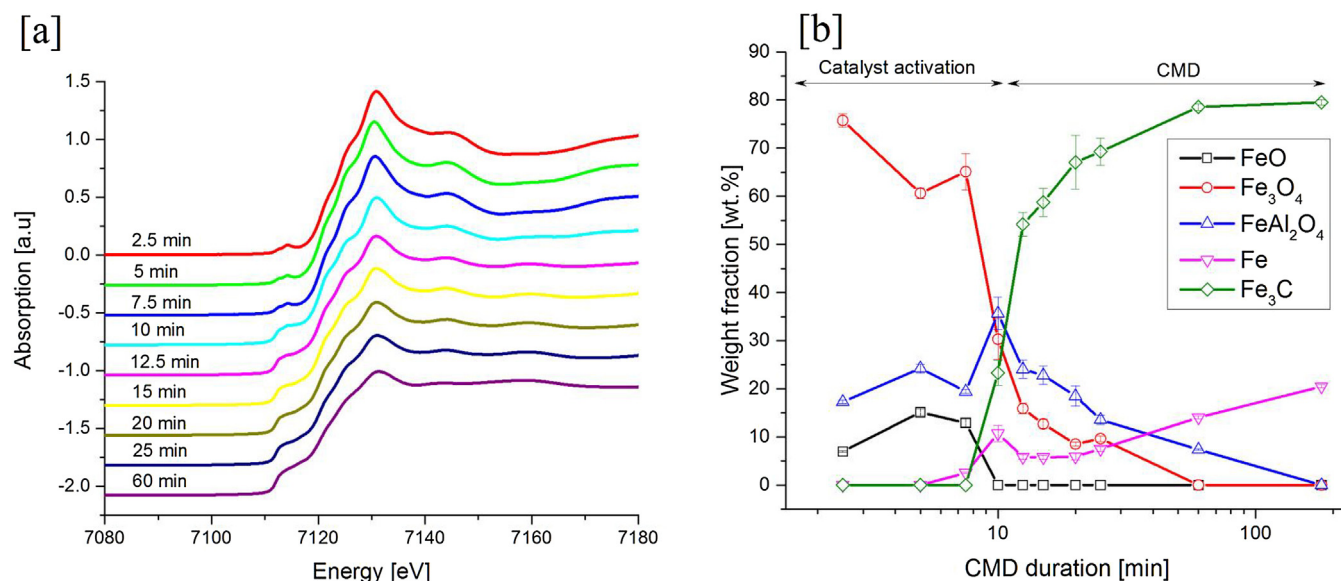
Fig. 14. a) Ex-situ Fe K-edge XANES spectra for the catalytic decomposition of methane using fused Fe_2O_3/Al_2O_3 as a pre-catalyst. b) Evolution of the sample composition as a function of time as calculated from linear combination fitting with spectra of Fe, Fe_3C, Fe_3O_4, $FeAl_2O_4$ and FeO standards.

3.3.3. Carbon morphologies over f-Fe_{65}-$Al_{3.7}$ after CMD

The surface morphologies of spent samples after CMD reaction at different SV are observed by TEM in Fig. 15. For the sample after CMD at the lowest SV of 1.875 L/g_{cat} h shown in Fig. 15(**a–e**), although the shapes are varied from straight (Fig. 15(**c**)) and bamboo-like (Fig. 15(**d**)(**e**)), most of them are bamboo-like CNTs have a hollow channel while holding Fe_3C particles on the end side (Fig. 15(**b**)). By increasing the SV, Fe_3C particles are observed to be progressively trapped into bamboo-like CNTs cage (Fig. 15(**f** and **g**)). Some CNOs (thick layer of graphite encapsulating Fe_3C) can even be seen over spent samples tested at SV of 15 L/g_{cat} h (Fig. 15(**h–j**)). Obviously, the SV increment will not change the reaction mechanism to produce a different phase, which suggests that the morphology of deposited carbon on f-Fe_{65}-$Al_{3.7}$ is not controlled by the catalyst crystalline structure, but by the reaction conditions. The morphology of deposited carbon on Ni catalysts for CMD was reported to be strongly influenced by its diffusion-graphite formation rate in our previous study [8]. As reported in [5], carbon materials with various morphologies, i.e., herringbone carbon nanofibers (CNFs), platelet CNFs, bamboo-shaped CNFs, branched CNFs, multi-branched CNFs and onion-like carbons, depending on the catalyst composition and reaction temperature, were obtained over Ni/CNT and Ni-Cu/CNT catalysts. The morphology of the produced carbon material was correlated with the growth mechanism of the carbon material on the catalyst. Similar model is also illustrated on f-Fe_{65}-$Al_{3.7}$ in this study as shown in Fig. 12(**f–h**). Normally, the continues CMD reaction on the Fe catalysts makes carbon precipitate out and crystallize in the form of a cylindrical network on the surface of the catalyst particle and finally grow into tubular structures, i.e. CNTs as shown in Fig. 12(**f**). Meanwhile, a special CNTs named as bamboo-shape tubes with Fe_3C on one side can also be formed in large amount over f-Fe_{65}-$Al_{3.7}$. When increasing the reaction SV, i.e., accelerating the graphite precipitation rate, a new type of bamboo-shape CNTs with Fe_3C trapped into the cavity is formed by the mechanism illustrated in Fig. 12(**g**). "Jumps" of the catalyst particles out of the graphite sheath to the top of the tube at regular time intervals was inferred by Y. Lu et al. [78] to explain the formation of bamboo-shaped CNTs with catalyst particle at tube end. The motive force of pushing out the catalyst particle may be a stress accumulated in the graphitic sheath due to the segregation of carbon from the inside of the sheath. It is

known that bulk Fe_3C melting point is about 300 °C below that of bulk Fe. Further, similar like the pure metal, the melting temperature of Fe_3C should become lower by decreasing its particle size [79]. Therefore, at the CMD reaction at 750 °C in this study, the Fe_3C with a size of 20–50 nm may perform at a quasi-liquid state. And therefore, with the growth of the CNTs, more and more parts of the catalyst particle were sucked into the tube, due to the compressive force formed at the bottom of the particles, which led to the "molten" Fe_3C becoming a cone shape. Meanwhile, because of the participated carbon lowered the exposed Fe_3C active surface towards CH_4, the transportation of carbon through the catalyst particle gradually decreased. Therefore, as explained by Luo et al. [80], when a compressive force from the preferential precipitation of carbon atoms decreased to such an extent that smaller than the surface tension of the catalyst particle, the portion of the sucked and stretched catalyst would be pulled back under the combined action of the surface tension of the particle and stress of the tube. In this way, a piece of bamboo was formed, and a new circle would start at the lower part of the catalyst particle, and produced another piece of bamboo. However, if the precipitation rate is accelerated a lot by increasing the SV, the stretched part of a particle could not be completely pulled back, a droplet of the catalyst particle would be kept in the compartment of the tube, and thus form bamboo-shape CNTs trapped Fe_3C. When the graphite precipitation rate is really very fast to make the compressive force overcome the surface tension of the Fe_3C, the latter (Fe_3C) will be totally encapsulated by the former (graphite) to form CNOs in Fig. 12(**h**).

4. Conclusions

Various types of Fe-based catalysts with different supports, additives and Fe loadings were synthesized by fusion and impregnation methods herein to investigate their CMD performance to produce H_2 and carbon nano materials. The followings are the conclusions summarized based on results and discussion.

1. Fused Fe (60 wt%) catalysts showed only Fe_2O_3 XRD reflection patterns as the additives oxides particles are assumed to be fine dispersed over Fe_2O_3 surface, while impregnated Fe (20 wt%) catalysts exhibited both patterns of Fe_2O_3 and corresponding supports.
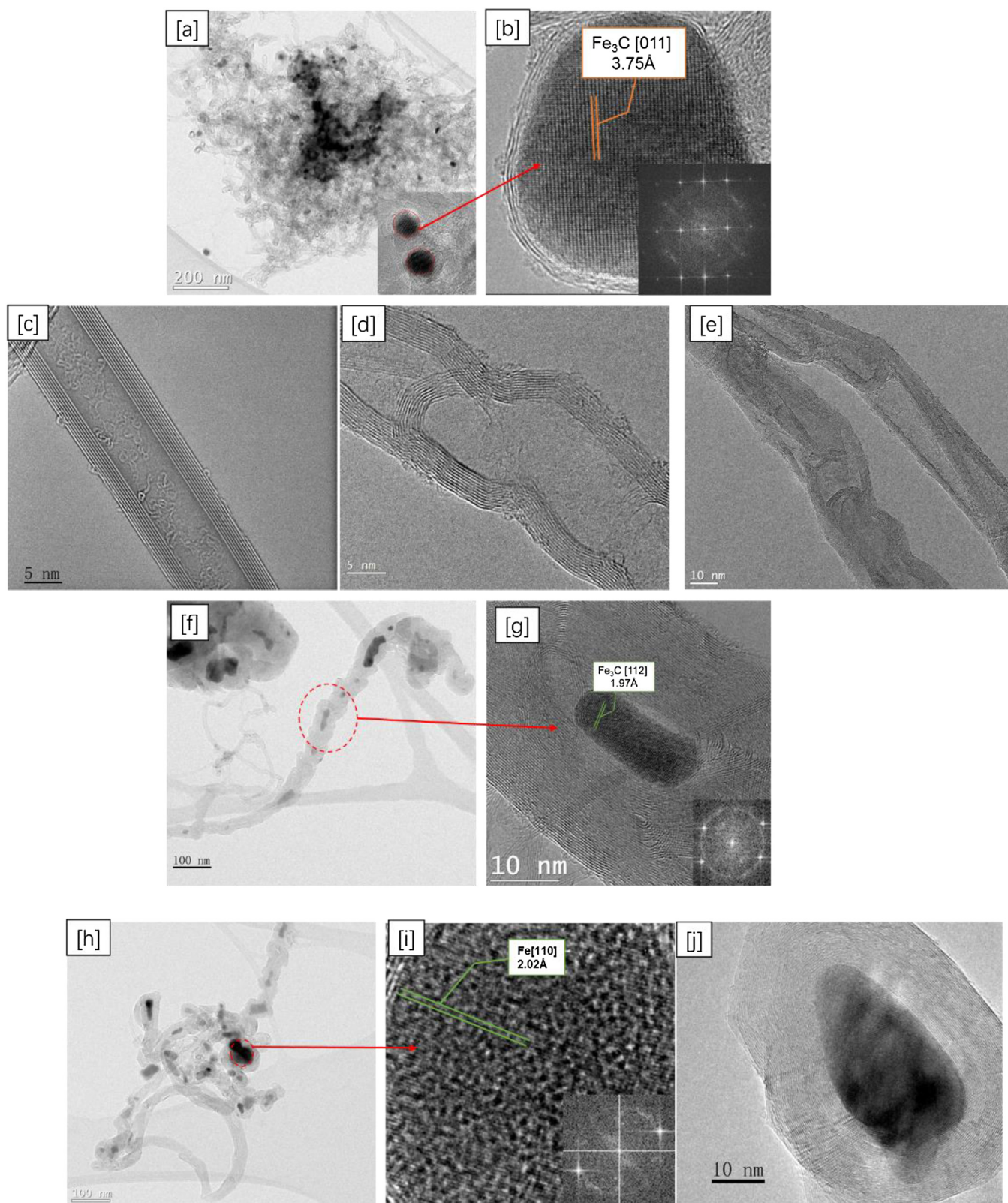
Fig. 15. CNT morphologies over spent catalysts after CMD at different SV in Fig. 10(a).

2. By H_2-TPR, both fused and impregnated samples follow the stepwise reduction mechanism as $Fe_2O_3 \rightarrow Fe_3O_4 \rightarrow FeO \rightarrow Fe^0$, while the interaction between Fe and supports would be reinforced to form solid solution during the thermal treatment higher than 450 °C.

3. Regardless preparation methods and Fe loading, Fe-Al_2O_3 catalysts showed the best CMD performance. Al_2O_3 is considered to affect Fe crystallization to expose more Fe^0 out of the surface area for the deposition of graphitic carbon. The selective forma-

tion of CNTs over Fe-Al$_2$O$_3$ catalysts is also speculated to be vital for their good CMD activity.

4. During CMD over Fe catalysts, DFT study together with XRD, TEM and EXAFS results indicated the simultaneous formation of Fe$_3$C and graphite C. The graphite is proposed to be spurted out from an unstable over-stoichiometric iron carbide Fe$_3$C$_{1+x}$ decomposition back to Fe$_3$C and C. A carbon deposition model was further built to explain the formation of different carbon nano materials.

5. Over f-Fe$_{65}$-Al$_{3.7}$ sample, 750 °C is concluded as the optimized temperature for pre-reduction with H$_2$ and CMD reaction to obtain a high CMD activity. At a low SV of 1.875 L/g$_{cat}$ h, this catalyst showed a stable methane conversion of c.a. 70% for as long as 400 min.

Acknowledgement

Appendix A. Supplementary data

Supplementary data associated with this article can be found, in the online version, at http://dx.doi.org/10.1016/j.apcatb.2017.02.052.

References

[1] S. Anderson, R. Newell, Prospects for carbon capture and storage technologies, Annu. Rev. Environ. Resour. 29 (2004) 109–142.
[2] J. Hetland, G. Mulder, In search of a sustainable hydrogen economy: how a large-scale transition to hydrogen may affect the primary energy demand and greenhouse gas emissions, Int. J. Hydrogen Energy 32 (2007) 736–747.
[3] A.C. Lua, H.Y. Wang, Hydrogen production by catalytic decomposition of methane over Ni-Cu-Co alloy particles, Appl. Catal. B—Environ. 156 (2014) 84–93.
[4] T.V. Choudhary, C. Sivadinarayana, C.C. Chusuei, A. Klinghoffer, D.W. Goodman, Hydrogen production via catalytic decomposition of methane, J. Catal. 199 (2001) 9–18.
[5] Y. Shen, A.C. Lua, Synthesis of Ni and Ni-Cu supported on carbon nanotubes for hydrogen and carbon production by catalytic decomposition of methane, Appl. Catal. B—Environ. 164 (2015) 61–69.
[6] D. Kang, J.W. Lee, Enhanced methane decomposition over nickel-carbon-B$_2$O$_3$ core-shell catalysts derived from carbon dioxide, Appl. Catal. B—Environ. 186 (2016) 41–55.
[7] A.C. Lua, H.Y. Wang, Decomposition of methane over unsupported porous nickel and alloy catalyst, Appl. Catal. B—Environ. 132 (2013) 469–478.
[8] L. Zhou, Y. Guo, K. Hideo, Unsupported nickel catalysts for methane catalytic decomposition into pure hydrogen, AIChE J. 60 (2014) 2907–2917.
[9] T. Koerts, M.J.A.G. Deelen, R.A. Vansanten, Hydrocarbon formation from methane by a low-temperature 2-Step reaction sequence, J. Catal. 138 (1992) 101–114.
[10] K. Nakagawa, M. Nishitani-Gamo, T. Ando, Hydrogen production from methane for fuel cell using oxidized diamond-supported catalysts, Int. J. Hydrogen Energy 30 (2005) 201–207.
[11] N.M. Rodriguez, A review of catalytically grown carbon nanofibers, J. Mater. Res. 8 (1993) 3233–3250.
[12] Y. Li, B.C. Zhang, X.W. Xie, J.L. Liu, Y.D. Xu, W.J. Shen, Novel Ni catalysts for methane decomposition to hydrogen and carbon nanofibers, J. Catal. 238 (2006) 412–424.
[13] H.F. Abbas, W.M.A.W. Daud, Thermocatalytic decomposition of methane for hydrogen production using activated carbon catalyst: regeneration and characterization studies, Int. J. Hydrogen Energy 34 (2009) 8034–8045.
[14] J. Li, K.J. Smith, Methane decomposition and catalyst regeneration in a cyclic mode over supported Co and Ni catalysts, Appl. Catal. A—Gen. 349 (2008) 116–124.
[15] J.L. Pinilla, I. Suelves, R. Utrilla, M.E. Galvez, M.J. Lazaro, R. Moliner, Hydrogen production by thermo-catalytic decomposition of methane: regeneration of active carbons using CO2, J. Power Sources 169 (2007) 103–109.
[16] J.I. Villacampa, C. Royo, E. Romeo, J.A. Montoya, P. Del Angel, A. Monzon, Catalytic decomposition of methane over Ni-Al2O3 coprecipitated catalysts reaction and regeneration studies, Appl. Catal. A—Gen. 252 (2003) 363–383.
[17] K. Otsuka, S. Kobayashi, S. Takenaka, Decomposition and regeneration of methane in the absence and the presence of a hydrogen-absorbing alloy CaNi5, Appl. Catal. A—Gen. 190 (2000) 261–268.
[18] K. Otsuka, N. Nakajima, I. Yamanaka, Decomposition and regeneration of methane by hydrogen absorbing alloys, Chem. Lett. (1998) 873–874.
[19] H.Y. Wang, A.C. Lua, Methane decomposition using Ni-Cu alloy nano-particle catalysts and catalyst deactivation studies, Chem. Eng. J. 262 (2015) 1077–1089.

[20] C. Escobar, O.W. Perez-Lopez, Hydrogen production by methane decomposition over Cu-Co-Al mixed oxides activated under reaction conditions, Catal. Lett. 144 (2014) 796–804.
[21] N. Bayat, M. Rezaei, F. Meshkani, Hydrogen and carbon nanofibers synthesis by methane decomposition over Ni-Pd/Al$_2$O$_3$ catalyst, Int. J. Hydrogen Energy 41 (2016) 5494–5503.
[22] J.S. Prasad, V. Dhand, V. Himabindu, Y. Anjaneyulu, P.K. Jain, B. Padya, Production of hydrogen and carbon nanofibers through the decomposition of methane over activated carbon supported Pd catalysts, Int. J. Hydrogen Energy 35 (2010) 10977–10983.
[23] S. Takenaka, Y. Shigeta, E. Tanabe, K. Otsuka, Methane decomposition into hydrogen and carbon nanofibers over supported Pd-Ni catalysts: characterization of the catalysts during the reaction, J. Phys. Chem. B 108 (2004) 7656–7664.
[24] A.E. Awadallah, M.S. Abdel-Mottaleb, A.A. Aboul-Enein, M.M. Yonis, A.K. Aboul-Gheit, Catalytic decomposition of natural gas to CO/CO$_2$-free hydrogen production and carbon nanomaterials using mgO-Supported monometallic iron family catalysts, Chem. Eng. Commun. 202 (2015) 163–174.
[25] G. Wang, Y. Jin, G. Liu, Y. Li, Production of hydrogen and nanocarbon from catalytic decomposition of methane over a Ni–Fe/Al$_2$O$_3$ catalyst, Energy Fuel 27 (2013) 4448–4456.
[26] D. Torres, S. de Llobet, J.L. Pinilla, M.J. Lazaro, I. Suelves, R. Moliner, Hydrogen production by catalytic decomposition of methane using a Fe-based catalyst in a fluidized bed reactor, J. Nat. Gas Chem. 21 (2012) 367–373.
[27] W.H. Wang, H.Y. Wang, Y. Yang, S.B. Jiang, Ni-SiO2 and Ni-Fe-SiO2 catalysts for methane decomposition to prepare hydrogen and carbon filaments, Int. J. Hydrogen Energy 37 (2012) 9058–9066.
[28] J.L. Pinilla, R. Utrilla, R.K. Karn, I. Suelves, M.J. Lazaro, R. Moliner, A.B. Garcia, J.N. Rouzaud, High temperature iron-based catalysts for hydrogen and nanostructured carbon production by methane decomposition, Int. J. Hydrogen Energy 36 (2011) 7832–7843.
[29] L.G. Tang, D. Yamaguchi, N. Burke, D. Trimm, K. Chiang, Methane decomposition over ceria modified iron catalysts, Catal. Commun. 11 (2010) 1215–1219.
[30] A.F. Cunha, J.J.M. Orfao, J.L. Figueiredo, Methane decomposition on Fe-Cu raney-type catalysts, Fuel Process. Technol. 90 (2009) 1234–1240.
[31] L. Zhou, L.R. Enakonda, Y. Saih, S. Loptain, D. Gary, P. Del-Gallo, J.-M. Basset, Catalytic methane decomposition over Fe-Al$_2$O$_3$, ChemSusChem (2016).
[32] A.M. Alvarez, S.G. Marchetti, M.V. Cagnoli, J.F. Bengoa, R.C. Mercader, A.A. Yeramian, Study of the Fe/zeolite-L system – part II: CO and H$_2$ chemisorption behavior, Appl. Surf. Sci. 165 (2000) 100–108.
[33] E.R. Malinowski, Factor Analysis in Chemistry, 2nd edition, Wiley-Interscience, 1991.
[34] G. Meitzner, E.S. Huang, Analysis of mixtures of compounds of copper using K-edge X-ray absorption-spectroscopy, Fresen. J. Anal. Chem. 342 (1992) 61–64.
[35] L. Reddy Enakonda, L. Zhou, Y. Saih, S. Ould-Chikh, S. Lopatin, D. Gary, P. Del-Gallo, J.-M. Basset, Methane-induced activation mechanism of fused ferric oxide-alumina catalysts during methane decomposition, ChemSusChem (2016).
[36] M.A. Marcus, A.J. Westphal, S.C. Fakra, Classification of Fe-bearing species from K-edge XANES data using two-parameter correlation plots, J. Synchrotron Radiat. 15 (2008) 463–468.
[37] X. Zhang, Y.G. Niu, Y. Li, X.M. Hou, Y.B. Wang, R. Bai, J.P. Zhao, Synthesis, optical and magnetic properties of alpha-Fe$_2$O$_3$ nanoparticles with various shapes, Mater. Lett. 99 (2013) 111–114.
[38] C. Laurent, A. Peigney, E. Flahaut, A. Rousset, Synthesis of carbon nanotubes-Fe-Al$_2$O$_3$ powders. Influence of the characteristics of the starting Al$_{1.8}$Fe$_{0.2}$O$_3$ oxide solid solution, Mater. Res. Bull. 35 (2000) 661–673.
[39] J.S. Yoo, A.A. Bhattacharyya, C.A. Radlowski, J.A. Karch, De-Sox catalyst – the role of iron in iron mixed solid-solution spinels, mgo.Mgal2-Xfexo4, Ind. Eng. Chem. Res. 31 (1992) 1252–1258.
[40] A.B. Peltekov, B.S. Boyanov, Study of solid state interactions in the systems ZnFe2O4-CaO, ZnFe2O4-MgO and zinc cake with CaO and MgO, J. Min. Metall. B 49 (2013) 339–346.
[41] M. Charilaou, J.F. Loffler, A.U. Gehring, Fe-Ti-O exchange at high temperature and thermal hysteresis, Geophys. J. Int. 185 (2011) 647–652.
[42] K.Z. Li, H. Wang, Y.G. Wei, D.X. Yan, Transformation of methane into synthesis gas using the redox property of Ce-Fe mixed oxides: effect of calcination temperature, Int. J. Hydrogen Energy 36 (2011) 3471–3482.
[43] M. del Arco, R. Trujillano, V. Rives, Cobalt-iron hydroxycarbonates and their evolution to mixed oxides with spinel structure, J. Mater. Chem. 8 (1998) 761–767.
[44] P. Hirunsit, K. Faungnawakij, Cu-Cr, Cu-Mn, and Cu-Fe spinel-oxide-type catalysts for reforming of oxygenated hydrocarbons, J. Phys. Chem. C 117 (2013) 23757–23765.
[45] G.F. Li, Q.Y. Wang, B. Zhao, M.Q. Shen, R.X. Zhou, Effect of iron doping into CeO$_2$-ZrO$_2$ on the properties and catalytic behaviour of Pd-only three-way catalyst for automotive emission control, J. Hazard. Mater. 186 (2011) 911–920.
[46] M.N. Cele, H.B. Friedrich, M.D. Bala, A study of Fe(III)TPPCl encapsulated in zeolite NaY and Fe(III)NaY in the oxidation of n-octane cyclohexane, 1-octene and 4-octene, React. Kinet. Mech. Cat. 111 (2014) 737–750.
[47] J. Zielinski, I. Zglinicka, L. Znak, Z. Kaszkur, Reduction of Fe$_2$O$_3$ with hydrogen, Appl. Catal. A—Gen. 381 (2010) 191–196.

[48] O.O. James, B. Chowdhury, S. Maity, TPR and TPD studies of effects of Cu and Ca promotion on Fe-Zn-based Fischer-Tropsch catalysts, J. Chem. Sci. 125 (2013) 679–686.

[49] G.K. Reddy, K. Gunasekera, P. Boolchand, J.H. Dong, P.G. Smirniotis, High temperature water gas shift reaction over nanocrystalline copper codoped-modified ferrites, J. Phys. Chem. C 115 (2011) 7586–7595.

[50] R.J. Kalenczuk, Study on the properties of iron-cobalt alumina-supported catalyst for ammonia, J. Chem. Technol. Biot. 59 (1994) 73–81.

[51] F.D. Liu, H. He, C.B. Zhang, Z.C. Feng, L.R. Zheng, Y.N. Xie, T.D. Hu, Selective catalytic reduction of NO with NH_3 over iron titanate catalyst: catalytic performance and characterization, Appl. Catal. B—Environ. 96 (2010) 408–420.

[52] L. Sun, X. Zhang, L. Chen, B. Zhao, S. Yang, X. Xie, Effects of Fe contents on fast pyrolysis of biomass with Fe/CaO catalysts, J. Anal. Appl. Pyrol. (2016).

[53] J. Beckers, G. Rothenberg, Redox properties of doped and supported copper-ceria catalysts, Dalton Trans. (2008) 6573–6578.

[54] R.L. Oliveira, I.G. Bitencourt, F.B. Passos, Partial oxidation of methane to syngas on Rh/Al_2O_3 and $Rh/Ce-ZrO_2$ catalysts, J. Braz. Chem. Soc. 24 (2013) 68–75.

[55] L. Zhou, L.D. Li, N.N. Wei, J. Li, J.M. Basset, Effect of $NiAl_2O_4$ formation on Ni/Al_2O_3 stability during dry reforming of methane, Chemcatchem 7 (2015) 2508–2516.

[56] H. Kathyayini, N. Nagaraju, A. Fonseca, J.B. Nagy, Catalytic activity of Fe, Co and Fe/Co supported on Ca and Mg oxides, hydroxides and carbonates in the synthesis of carbon nanotubes, J. Mol. Catal. A—Chem. 223 (2004) 129–136.

[57] A.H. Fakeeha, A.A. Ibrahim, M.A. Naeem, W.U. Khan, A.E. Abasaeed, R.L. Alotaibi, A.S. Al-Fatesh, Methane decomposition over Fe supported catalysts for hydrogen and nano carbon yield, Catal. Sustain. Energy 2 (2015) 71–82.

[58] A.A. Ibrahim, A.S. Al-Fatesh, W.U. Khan, M.A. Soliman, R.L. Al Otaibi, A.H. Fakeeha, Influence of support type and metal loading in methane decomposition over iron catalyst for hydrogen production, J. Chin. Chem. Soc.—Taip. 62 (2015) 592–599.

[59] L.B. Avdeeva, T.V. Reshetenko, Z.R. Ismagilov, V.A. Likholobov, Iron-containing catalysts of methane decomposition: accumulation of filamentous carbon, Appl. Catal. A—Gen. 228 (2002) 53–63.

[60] T.V. Reshetenko, L.B. Avdeeva, V.A. Ushakov, E.M. Moroz, A.N. Shmakov, V.V. Kriventsov, D.I. Kochubey, Y.T. Pavlyukhin, A.L. Chuvilin, Z.R. Ismagilov, Coprecipitated iron-containing catalysts ($Fe-Al_2O_3$, $Fe-Co-Al_2O_3$ $Fe-Ni-Al_2O_3$) for methane decomposition at moderate temperatures − Part II. Evolution of the catalysts in reaction, Appl. Catal. A—Gen. 270 (2004) 87–99.

[61] S. Takenaka, M. Serizawa, K. Otsuka, Formation of filamentous carbons over supported Fe catalysts through methane decomposition, J. Catal. 222 (2004) 520–531.

[62] X.X. Li, G.L. Zhu, S.T. Qi, J. Huang, B.L. Yang, Simultaneous production of hythane and carbon nanotubes via catalytic decomposition of methane with catalysts dispersed on porous supports, Appl. Energy 130 (2014) 846–852.

[63] L. Zhou, J.M. Basset, Unsupported NiPt alloy metal catalysts prepared by water-in-oil (W/O) microemulsion method for methane cracking, Fuel 181 (2016) 805–810.

[64] R.J. Wrobel, A. Helminiak, W. Arabczyk, U. Narkiewicz, Studies on the kinetics of carbon deposit formation on nanocrystalline iron stabilized with structural promoters, J. Phys. Chem. C 118 (2014) 15434–15439.

[65] L. Ni, K. Kuroda, L.P. Zhou, K. Ohta, K. Matsuishi, J. Nakamura, Decomposition of metal carbides as an elementary step of carbon nanotube synthesis, Carbon 47 (2009) 3054–3062.

[66] V.I. Zaikovskii, V.V. Chesnokov, R.A. Buyanov, Formation of carbon filaments from 1,3-butadiene on Fe/Al_2O_3 catalysts, Kinet. Catal. 43 (2002) 677–683.

[67] A.K. Schaper, H.Q. Hou, A. Greiner, F. Phillipp, The role of iron carbide in multiwalled carbon nanotube growth, J. Catal. 222 (2004) 250–254.

[68] G. Kresse, J. Furthmüller, Efficiency of ab-initio total energy calculations for metals and semiconductors using a plane-wave basis set, Comput. Mater. Sci. 6 (1996) 15–50.

[69] G. Kresse, D. Joubert, From ultrasoft pseudopotentials to the projector augmented-wave method, Phys. Rev. B 59 (1999) 1758–1775.

[70] J.P. Perdew, K. Burke, M. Ernzerhof, Generalized gradient approximation made simple, Phys. Rev. Lett. 77 (1996) 3865–3868.

[71] P.E. Blöchl, Projector augmented-wave method, Phys. Rev. B 50 (1994) 17953–17979.

[72] H.J. Monkhorst, J.D. Pack, Special points for Brillouin-zone integrations, Phys. Rev. B 13 (1976) 5188–5192.

[73] M. Hasebe, H. Ohtani, T. Nishizawa, Effect of magnetic transition on solubility of carbon in bcc Fe and fcc Co-Ni alloys, Metall. Trans. A 16 (1985) 913–921.

[74] C.T. Wirth, B.C. Bayer, A.D. Gamalski, S. Esconjauregui, R.S. Weatherup, C. Ducati, C. Baehtz, J. Robertson, S. Hofmann, The phase of iron catalyst nanoparticles during carbon nanotube growth, Chem. Mater. 24 (2012) 4633–4640.

[75] R. Sharma, E. Moore, P. Rez, M.M.J. Treacy, Site-specific fabrication of Fe particles for carbon nanotube growth, Nano Lett. 9 (2009) 689–694.

[76] F. de Groot, G. Vanko, P. Glatzel, The 1s x-ray absorption pre-edge structures in transition metal oxides, J. Phys.-Condens. Mater. 21 (2009).

[77] D. Cabaret, A. Bordage, A. Juhin, M. Arfaoui, E. Gaudry, First-principles calculations of X-ray absorption spectra at the K-edge of 3d transition metals: an electronic structure analysis of the pre-edge, Phys. Chem. Chem. Phys. 12 (2010) 5619–5633.

[78] Y. Lu, Z.P. Zhu, D.S. Su, D. Wang, Z.Y. Liu, R. Schlogl, Formation of bamboo-shape carbon nanotubes by controlled rapid decomposition of picric acid, Carbon 42 (2004) 3199–3207.

[79] L. Pellegrino, M. Daghetta, R. Pelosato, A. Citterio, C.V. Mazzocchia, Searching for rate determining step of CNT formation: the role of cementite, Chem. Eng. Trans. 32 (2013) 739–744.

[80] C.Z. Luo, Q. Fu, C.X. Pan, Strong magnetic field-assisted growth of carbon nanofibers and its microstructural transformation mechanism, Sci. Rep.—UK 5 (2015).